

Comparing 1-year GUMICS–4 simulations of the Terrestrial Magnetosphere with Cluster Measurements

G. Facskó^{1,2,3}, D. G. Sibeck², I. Honkonen⁴, L. Degener^{4*}, P. Peitso^{5†},
E. I. Tanskanen⁵, C. R. Anekallu⁶, J. Kalmár⁷, J. Bór⁷, G. Farinas Perez^{2,3‡},
S. Szalai⁷, Á. Kis⁷, V. Wesztergom⁷

¹Wigner Research Centre for Physics, Budapest, Hungary

²NASA Goddard Space Flight Center, Greenbelt, Maryland, USA

³the Catholic University of America, Washington DC, USA

⁴Finnish Meteorological Institute, Helsinki, Finland

⁵Aalto University, School of Electrical Engineering, Espoo, Finland

⁶UCL Department of Space & Climate Physics, Mullard Space Science Laboratory, Dorking, UK

⁷Research Centre for Astronomy and Earth Sciences, Sopron, Hungary

Key Points:

- The GUMICS–4 provides realistic ion plasma moments and magnetic field in the solar wind and the outer magnetosheath.
- The code can predict the realistic location of the bow shock.
- An inner magnetosphere model should be added to the code to increase the accuracy of the simulation.

*Now private individual, Hannover, Germany

†Now at Aurora Propulsion Technologies, Espoo, Finland

‡Now at University of Miami, Electrical and Computer Engineering Department, Miami, Florida, USA

Corresponding author: Gábor Facskó, gabor.i.facsko@gmail.com

19 **Abstract**

20 Previously a 1-year global magnetohydrodynamics simulation was made using the GUMICS–4
 21 code and the OMNI 1-min resolution solar wind data from January 29, 2002 to Febru-
 22 ary 2, 2003 as input. **From the saved simulation results parameters were dumpped**
 23 along the orbit of the Cluster SC3 reference spacecraft **to create a special product**
 24 **for further studies and validations.** We compare the saved parameters with the Clus-
 25 ter SC3 measurements. We use the magnetic field Z component, the solar wind veloci-
 26 ty X component and the solar wind density of the Cluster magnetometer, ion plasma
 27 and spacecraft potential measurements **in the** geocentric solar ecliptic reference frame,
 28 **respectively.** We select intervals in the solar wind, the magnetosheath and the mag-
 29 netosphere where the instruments above provided good quality data and the spacecraft
 30 and the simulation are in the same region. We determine the location of the bow shock,
 31 the magnetopause and the neutral sheet in the spacecraft measurements and compare
 32 their position in the observation and simulations.

33 The GUMICS–4 provides quite good results in the solar wind however its accu-
 34 racy is **worse** in the magnetosheath. The simulation results are not realistic in the mag-
 35 netosphere. The bow shock location is predicted well however the magnetopause loca-
 36 tion is less accurate. The neutral sheet positions are located quite well thanks to the spe-
 37 cial solar wind conditions. The reason for **the inaccuracy of the magnetopause po-**
 38 **sition and the parameters of the magnetosphere** is the missing inner magneto-
 39 sphere model.

40 **1 Introduction**

41 **One of the** most cost-effective way to study the interaction of the solar wind and
 42 the planetary magnetospheres (or predict the conditions of the near-Earth space) is us-
 43 ing a global magnetohydrodynamic (MHD) code. In the past, several [...] parallelized,
 44 effective, verified and validated codes were developed, which are used and applied to fore-
 45 cast the cosmic environment of the Earth; such as the Lyon-Fedder-Mobarry [LFM; *Lyon*
 46 *et al.*, 2004] code, the Open Geospace General Circulation Model [OpenGGCM; *Raeder*
 47 *et al.*, 2008], the Block-Adaptive-Tree-Solarwind-Roe-Upwind-Scheme [BATS-R-US; *Pow-*
 48 *ell et al.*, 1999; *Tóth et al.*, 2012]. In Europe only three global MHD codes were devel-
 49 oped: the Grand Unified Magnetosphere–Ionosphere Coupling Simulation [GUMICS–4;
 50 *Janhunen et al.*, 2012], the Computational Object Oriented Libraries for Fluid Dynam-

ics [COOLFluiD; *Lani et al.*, 2012] and the 3D resistive magnetohydrodynamic code Gorgon [*Chittenden et al.*, 2004; *Ciardi et al.*, 2007]. The COOLFluiD is a general-purpose plasma simulation tool. The Gorgon code was developed for studying high energy, collisional plasma interactions and has been adapted to simulate planetary magnetospheres and their interaction with the solar wind [*Mejnertsen et al.*, 2016, 2018]. **Neither Gorgon nor COOLfluid have an ionospheric solver.** The GUMICS–4 was developed to study the solar wind-terrestrial magnetosphere interaction and its parallel version has not been available for the scientific community **because it is still in development** (see Section 2.1). These codes are available at the Community Coordinated Modelling Center (CCMC; <http://ccmc.gsfc.nasa.gov/>) hosted by the NASA Goddard Space Flight Center (GSFC) **or** the Virtual Space Weather Modelling Centre (VSWMC; [http://swe.ssa.esa.int/web/guest/kul-cmpa-federated; requires registration for the European Space Agency \(ESA\) Space Situational Awareness \(SSA\) Space Weather \(SWE\) portal](http://swe.ssa.esa.int/web/guest/kul-cmpa-federated; requires registration for the European Space Agency (ESA) Space Situational Awareness (SSA) Space Weather (SWE) portal)) hosted by the KU Leuven [*Poedts et al.*, 2020]. The comparison of the simulation results to space-craft and ground-based measurements is necessary to understand the abilities and features of the developed tools. The statistical study using long term global MHD runs for validation [...] of the codes seems to be a good and fruitful method. However, providing long simulations is costly and time consuming hence only a few studies were done previously using much shorter simulations than a year.

Guild et al. [2008a,b] launched two months of LFM run and compared the plasma sheet properties in the simulated tail with the statistical properties of six years Geotail magnetic field and plasma observations [*Kokubun et al.*, 1994; *Mukai et al.*, 1994]. The LFM successfully reproduced the global features of the global plasma sheet in statistical sense. However, there were some differences. The sheet was too cold, too dense and the bulk flow was faster than the observed plasma sheet. The LFM overestimated the ionospheric transpolar potential. The transpolar potential correlated with the speed of the plasma sheet flows. The equatorial maps of density, thermal pressure, thermal energy and velocity were compared. The LFM overestimated the plasma sheet density close to the Earth and underestimated the temperature by a factor of ~ 3 . The LFM overestimated the global average flow speed by a factor of ~ 2 . The LFM reproduced many of the climatological features of the Geotail data set. The low-resolution model underestimated the occurrence of the fast earthward and tailward flows. Increasing the simu-

83 lation resolution resulted in the development of fast, busty flows. These flows contributed
 84 to the statistics and brought the simulations to the observations closer.

85 *Zhang et al.* [2011] [...] studied the statistics of magnetosphere-ionosphere (MI)
 86 coupling **using *Guild et al.* [2008a]’s LFM simulation above.** The polar cap po-
 87 tential and the field aligned currents (FAC), the downward Poynting flux and the vor-
 88 ticity of the ionospheric convection were compared with observed statistical averages and
 89 the Weimer05 empirical model [*Weimer*, 2005]. The comparisons showed that the LFM
 90 model produced quite accurate average distributions of the Region 1 (R1) and Region
 91 2 (R2) currents. The ionospheric Region 2 currents in the MHD simulation seemed to
 92 be originated from the diamagnetic ring current. The average LFM Region 1 and 2 cur-
 93 rents were smaller compared with the values from the Weimer05 model. The average CPCP
 94 was higher in the LFM simulation than the measurements of the SuperDARN and the
 95 Weimer05 model. The average convention pattern was quite symmetric in the LFM sim-
 96 ulation against the SuperDARN measurements and the Weimer05 model. The Super-
 97 DARN measurements and the Weimer05 model had dawn-dusk asymmetry. In the LFM
 98 model more Poynting flux flowed into the polar region ionosphere than in the Weimer05
 99 model. It was the consequence of the larger CPCP in the LFM simulation. The larger
 100 CPCP allowed higher electric field in the polar region. The statistical dependence of the
 101 high-latitude convection patterns on Interplanetary Magnetic Field (IMF) clock angle
 102 was similar to the SuperDARN measurements [*Sofko et al.*, 1995] and the Weimer05 model.
 103 The average ionospheric field-aligned vorticity showed good agreement on the dayside.
 104 However, the LFM model gave larger nightside vorticity than SuperDARN measurements
 105 because the Pedersen conductance on the night side ionosphere was too low.

106 *Wiltberger et al.* [2017] studied the structure of the high latitude field-aligned cur-
 107 rent patterns using three resolutions of the LFM global MHD code and the Weimer05
 108 empirical model [*Weimer*, 2005]. The studied period was a month long and contained
 109 two high-speed streams. Generally, the patterns agreed well with results obtained from
 110 the Weimer05 computing. As the resolution of the simulations increased, the currents be-
 111 came more intense and narrow. The ratio of the Region 1 (R1), the Region 2 (R2) cur-
 112 rents and the R1/R2 ratio increased when the simulation resolution increases. However,
 113 both the R1 and R2 currents were smaller than the predictions of the Weimer05 model.
 114 This effect led to a better agreement of the LFM simulation results with the Weimer 2005
 115 model results. The CPCP pattern became concentrated in higher latitudes because of

116 the stronger R2 currents. The relationship of the CPCP and the R1 looked evident at
 117 higher resolution of the simulation. The LFM simulation could have reproduced the sta-
 118 tistical features of the field aligned current (FAC) patterns.

119 *Hajducek et al. [2017]* simulated a month of January 2005 using the Space Weather
 120 Modelling Framework [SWMF; *Tóth et al.*, 2005] and the OMNI solar wind data as in-
 121 put. The simulations were done with and without inner magnetosphere model and us-
 122 ing two different grid resolutions. The model was very good in predicting the **ring** cur-
 123 rents [...] [SYM-H; <http://wdc.kugi.kyoto-u.ac.jp/aeasy/asy.pdf>; *Iyemori*, 1990]. The
 124 K_p index (that measures the general magnetospheric convention and the auroral currents
 125 [*Bartels et al.*, 1939; *Rostoker*, 1972; *Thomsen*, 2004]) was predicted well during storms
 126 however the index was over predicted during quiet time periods. The AL index (that de-
 127 scribes the westward electro jet of the surface magnetic field introduced by *Davis and*
 128 *Sugiura* [1966]) was predicted reasonably well in average however the model reached the
 129 highest negative AL value less often than the observations because the model captured
 130 the structure of the auroral zone currents poorly. The overpredicting of K_p index dur-
 131 ing quiet times might have had the same reason because that index was also sensitive
 132 for the auroral zone dynamics. The SWMF usually over predicted the CPCP. These re-
 133 sults were not sensitive to grid resolutions. Except that the AL index reached the high-
 134 est negative value more often when the grid resolution was higher. Switching off of the
 135 inner magnetosphere model had dramatic effect for the accuracy of all quantities men-
 136 tioned above, except the CPCP.

137 In this paper the Cluster SC3 measurements are compared directly to a previously
 138 made 1-year long GUMICS–4 simulation in the solar wind, magnetosheath and the mag-
 139 netosphere along the Cluster SC3 orbit saved from the simulation results and measured
 140 by the spacecraft [*Facskó et al.*, 2016]. Three parameters (B_z , V_X and n) were studied
 141 as well as the location of the bow shock, magnetopause and the neutral sheet. The struc-
 142 ture of this paper is as follows. Section 2 describes the GUMICS–4 code, the 1-year sim-
 143 ulation and the instruments. Section 3 gives comparisons between the simulations and
 144 observations. Results of the comparison are discussed in Section 4. Finally, Section 5 con-
 145 tains the conclusions.

146 **2 The GUMICS–4 products and Cluster measurements**

147 Here we use two [...] very different [...] time series. The first **time series are**
 148 derived from a previously made 1-year GUMICS–4 simulation [*Facskó et al.*, 2016]. The
 149 second **time series were** measured by the magnetometer, ion plasma and electric field
 150 instruments of the Cluster reference spacecraft.

151 **2.1 The GUMICS–4 code**

152 The GUMICS–4 has two coupled simulation domains, the magnetospheric domain
 153 outside of $3.7 R_E$ radius around the Earth and a coupled ionosphere module containing
 154 a 3D electron density model of the ionosphere. The GUMICS–4 is not a parallel code
 155 however it was extensively used for studying the energy propagation processes from the
 156 solar wind to the magnetosphere through the magnetopause and other features [*Janhunen*
 157 *et al.*, 2012, see the references therein]. The code has also been applied for studying the
 158 forced reconnection in the tail [*Vörös et al.*, 2014]. Recently a few hundreds of synthetic
 159 two hours duration GUMICS–4 simulations were made to compare the simulation re-
 160 sults to empirical formulas [*Gordeev et al.*, 2013]. The agreement was quite good how-
 161 ever the diameter of the magnetopause deviated significantly in the simulation and the
 162 observations in the tail. The tail of the GUMICS–4 was smaller than spacecraft observed
 163 and measured. A 1-year long simulation was made using the GUMICS–4 code [*Facskó*
 164 *et al.*, 2016]. *Juusola et al.* [2014] compared the ionospheric currents, fields and the cross
 165 polar cap potential (CPCP) in the simulation versus Super Dual Auroral Radar Network
 166 (SuperDARN) radars [*Greenwald et al.*, 1995] and CHAMP spacecraft [*Reigber et al.*,
 167 2002] field aligned currents (FAC) measurements [*Juusola et al.*, 2007; *Ritter et al.*, 2004].
 168 The agreement was good in the seasonal variation of the CPCP however the FAC and
 169 other currents could not be reproduced properly. The possible cause of this bad agree-
 170 ment could be the lack of the inner magnetosphere model. This statement is supported
 171 by the result of *Hajducek et al.* [2017]. *Hajducek et al.* simulated only a month using dif-
 172 ferent spatial resolution and to test the codes switched off the inner magnetosphere model
 173 of the SWMF for a special run. This run without inner magnetosphere model made it
 174 clear that only the CPCP parameter of the simulation agreed quite well with the mea-
 175 surement. This fact explained why the agreement between the Cluster SC3 and the GUMICS-
 176 4 simulations was so good as described by [*Lakka et al.*, 2018a,b] based on the CPCP
 177 in GUMICS–4 simulations. *Kallio and Facskó* [2015] determined the solar wind param-

eters along the Moon orbit using the results of the *Facskó et al.* [2016]’s global MHD simulations. The solar wind parameters differed significantly in the geotail that should have been considered in future studies of the interaction of the solar wind and the lunar orbit. *Facskó et al.* [2016] determined the footprint of the Cluster SC3 using the 1-year simulation and the Tsyganenko T96 empirical model [*Tsyganenko*, 1995]. The code seemed to react slower to the dynamic changes of the solar wind pressure than the empirical model. The agreement of the footprint is better in the Northern Hemisphere. The GUMICS–4 tail looked shorter in the simulations than the observations. Finally, the Y component of the interplanetary magnetic field twisted the simulated tail hence the agreement of the empirical and computational footprints was worse at such solar wind conditions.

A workpackage of the European Cluster Assimilation Technology (ECLAT) project (https://cordis.europa.eu/result/rcn/165813_en.html; <http://www.eclat-project.eu/>) was the creation and analysis of a 1-year global MHD simulation using the OMNI solar wind data from January 29, 2002 to February 2, 2003 as input of the GUMICS–4 code [*Facskó et al.*, 2016]. The GUMICS-4 was a single core system [*Janhunen et al.*, 2012] hence the 1-year simulation was made in 1860 independent runs. This interval covered 155 Cluster SC3 orbits and each orbit lasted 57 hours. The supercomputer had 12 CPUs on each node hence the 57 hours were divided into 4.7 hours simulation time with one hour initialisation period. Each sub-intervals used its own average Geocentric Solar Ecliptic (GSE) IMF magnetic field X component B_x component and dipole tilt angle. All data gaps of the input file were filled using interpolation. If the data gap of the input file was at the beginning (or the end) interval the first (or last) good data of the input file was used to fill the gap. The initialisation of each simulations was made using constant values. These values were the first valid data of the input file repeated 60 times (60 minutes) in the input file of the sub-interval. The simulation results were saved in every five minutes. Various simulation parameters, for example, the density, particle density, temperature, magnetic field, solar wind velocity (29 different quantities) were saved from the simulation results along the Cluster reference spacecraft in the GSE coordinates. In this paper these parameters, namely the B_z magnetic field GSE Z component, the solar wind velocity GSE X component (V_x) and the solar wind density n are compared to the Cluster SC3 measurement. These parameters are selected because the B_z controls the magnetosphere, the V_x is the main solar wind velocity component and the n is the ion plasma

210 momentum that is the easiest to calculate; furthermore more instruments could deter-
211 mine it (see Section 2.2).

212 2.2 The Cluster SC3 measurements

213 The Cluster-II spacecraft of the European Space Agency (ESA) were launched in
214 2000 and study the geospace since then [Credland *et al.*, 1997; Escoubet *et al.*, 2001]. Its
215 four spacecraft form a tetrahedron however here we use only the measurements of the
216 reference spacecraft, the Cluster SC3. The spacecraft were stabilised by rotation and its
217 period is ~ 4 s. Hence, the temporal resolution of the plasma instruments were consid-
218 ered 4 s and we use 4 s averaged magnetic field data. The real resolution of the Cluster
219 FluxGate Magnetometer (FGM) magnetic field instrument was 27 Hz [Balogh *et al.*, 1997,
220 2001]. The ion plasma data was provided by the Cluster Ion Spectrometry (CIS) Hot
221 Ion Analyser (HIA) sub-instrument [Reme *et al.*, 1997; Rème *et al.*, 2001]. The CIS HIA
222 instrument is calibrated using the Waves of HIgh frequency Sounder for Probing the Elec-
223 tron density by Relaxation (WHISPER) wave instrument onboard Cluster [Décréau *et al.*,
224 2001; Trotignon *et al.*, 2010; Blagau *et al.*, 2013, 2014]. These calibrations might have
225 appeared as sudden non-physical jumps in the CIS HIA data. The CIS HIA had differ-
226 ent modes to measure in the solar wind and the magnetosphere. When the instrument
227 switched from a mode to another mode it appeared as a non-physical jump in the mea-
228 sured data too. These features had an influence on the accuracy of the data analysis.

229 We protect our results from these non-physical jumps described previously using
230 a density determination based on different principles. We use the spacecraft potential
231 of the Electric Field and Wave Experiment [EFW ; Gustafsson *et al.*, 1997, 2001] to de-
232 termine the electron density. This quantity can be calculated using the empirical den-
233 sity formula

$$n_{EFW} = 200(V_{sc})^{-1.85}, \quad (1)$$

234 where n_{EFW} is the calculated density and V_{sc} is the Cluster EFW spacecraft potential
235 [Trotignon *et al.*, 2010, 2011]. The EFW and the WHISPER were used for the calibra-
236 tion of the CIS HIA and the Plasma Electron and Current Experiment [PEACE; John-
237 stone *et al.*, 1997; Fazakerley *et al.*, 2010a,b]. Both instruments were still working on-
238 board all Cluster spacecraft. Their stable operation reduced the number of data gaps;
239 furthermore made the data analysis easier.

240 **3 Comparison of measurements to simulation**

241 The saved parameters from the GUMICS–4 simulations and the Cluster SC3 mag-
 242 netic field, solar wind velocity and density measurements are compared in the solar wind,
 243 magnetosheath and magnetosphere using cross correlation calculation. The resolution
 244 of the simulated Cluster orbit data is mostly five minutes because the simulations are
 245 saved in every five minutes [Facsikó *et al.*, 2016]. However, the time difference between
 246 points could be more than five minutes at the boundary of the subintervals, because the
 247 length of simulation intervals is determined in minutes. To facilitate analysis of the sim-
 248 ulation results, all simulation data were interpolated to one minute resolution. This method
 249 does not provide extra information to the cross correlation calculation. The data gaps
 250 are eliminated using interpolation in the data and extrapolation when the gap is at the
 251 start or the end of the selected interval. The spin resolution (4 s) of Cluster SC3 mag-
 252 netic field measurements is averaged over one minute around ($\pm 30\text{ s}$) the time stamps
 253 of the saved data.

254 For the correlation calculation intervals are selected carefully in the solar wind (see
 255 **Section 3.1**), the magnetosheath (see **Section 3.2**), the dayside and the night side mag-
 256 netosphere (see **Section 3.3**). In these intervals the parameters did not vary a lot and
 257 neither the Cluster nor the virtual probe crossed any boundary layers. To compare the
 258 shape of the B_z magnetic field, V_x solar wind speed and the n_{CIS} and the n_{EFW} curves
 259 we calculate cross correlation on selected intervals. Sometimes we get very bad results.
 260 Then we carefully examined the case and remove the short intervals (shorter than four
 261 hours) from the correlation calculation and large data gaps from the correlation calcu-
 262 lation. (The data gaps are interpolated however they cause loss of information.) Those
 263 intervals are also neglected where the plasma instrument has a calibration error or changes
 264 its mode from magnetosphere to solar wind (for example). The electron density is also
 265 calculated using the empirical density formula (see Equation 1) and making the corre-
 266 lation calculation. We want to avoid calibration errors and sudden non-physical jumps
 267 mentioned previously. The results do not differ significantly however the n_{EFW} does not
 268 have any mode change and it is applicable in the magnetosphere too (against the CIS
 269 HIA instrument).

270 **3.1 Solar wind**

271 We use OMNI IMF and solar wind velocity, density and temperature data as input
 272 of the simulation. Nevertheless, it is not useless to compare the solar wind region
 273 in the simulation and the measurements. The IMF X component cannot be given to the
 274 GUMICS–4 as input [Janhunen *et al.*, 2012; Fácskó *et al.*, 2016]. However the magnetic
 275 field of the solar wind has X component in the simulations. Additionally the solar wind
 276 structure might change from the simulation domain boundary at $+32 R_E$ to the sub-solar
 277 point of the terrestrial bow shock where all OMNI data is shifted. Almost the same so-
 278 lar wind intervals are used as in the see Table 1 of Fácskó *et al.* [2016]. The number of
 279 these intervals is small because the Cluster fleet instruments were calibrated in 2002, just
 280 after launching (Table 1). Hence we do not have a satisfactory ion plasma data cover-
 281 age for this year. Additionally, to improve the accuracy of the correlation calculation (see
 282 below) we delete the intervals that were too short (shorter than five hours) or the CIS
 283 HIA instrument changed its mode. The Cluster fleet is located in the solar wind only
 284 from December to May and only for a couple of hours during each orbit near to the apogee.
 285 We double check whether the Cluster SC3 stays in the solar wind in both the simula-
 286 tion and reality. We also check the omnidirectional CIS HIA ion spectra on the Clus-
 287 ter Science Archive (CSA; <https://www.cosmos.esa.int/web/csa/csds-quicklook-plots>).
 288 Hence 17 intervals are left in the solar wind to study (Figure 1).

289 The selected intervals have quiet solar wind conditions (Figure 2). The GUMICS–4
 290 simulation results have five minutes resolution and the Cluster SC3 measurements have
 291 one minute resolution (Figure 3). The measurements vary significantly. In spite of the
 292 quiet conditions the solar wind density often changes and deviates from the simulation.
 293 On Figure 4c both densities deviate significantly. The CIS HIA density deviation is larger
 294 as it is expected because of the complexity and the large number of working modes of
 295 the CIS instrument. The magnetic field and the solar wind velocity fit better. On Fig-
 296 ure 5a the correlation of the magnetic field is very good; furthermore on Figure 5c, 5e, 5f
 297 the correlation of the solar wind velocity and density is excellent (Table 1). The time
 298 shift on Figure 5b, Figure 5d, Figure 5f is about five minutes for the magnetic field and
 299 the CIS data. On Figure 5h for the EFW data the time shift is worse. It is not deter-
 300 mined as well as the other parameters.

301 **3.2 Magnetosheath**

302 The Cluster SC3 spent only a little time in the solar wind from December, 2002
 303 to May, 2003. However, the orbit of the spacecraft always crosses the magnetosheath (Figure 6). We selected intervals when the value of the magnetic field is around 25 nT. The
 304 field should be fluctuating because of the turbulent and deviated flow of the solar wind
 305 after passing the bow shock. In the same time the solar wind temperature increases. The
 306 solar wind speed drops hence its value is only 100-300 km/s. The density of the plasma
 307 flow increased and reached the $10\text{-}20 \text{ cm}^{-3}$. The narrow band on the omnidirectional CIS
 308 HIA ion spectra from the CSA (<https://www.cosmos.esa.int/web/csa/csds-quicklook-plots>) is widened after passing the bow shock. 15–30 minutes after this crossing we con-
 309 sidered the Cluster SC3 to enter into the magnetosheath. At the inner boundary **of the**
 310 **magnetopause** the flow speed drops and the density as well. The magnetic field starts
 311 growing and it is less turbulent than in the magnetosheath. The wide band on the the
 312 omnidirectional CIS HIA ion spectra disappears. 15–30 minutes before the appearance
 313 of these indicators of the magnetopause crossing our intervals end. All intervals contain
 314 large data gap, non-physical jump of instrument mode changing or shorter than four hour
 315 are removed. Hence 74 intervals considered in our final selection (Table 2).

318 All intervals have quiet upstream (or input) solar wind conditions (Figure 7). In
 319 [...] our selections the magnetic field and the plasma parameters and the calculated
 320 empirical density vary significantly stronger than in the solar wind intervals (Figure 8).
 321 The deviation of the simulated and the observed data is larger in this region as well. The
 322 scattered plots of the magnetic field, plasma flow speed and the densities agree well how-
 323 ever these plots are relatively less accurate than the scattered plots of the solar wind (Fig-
 324 ure 9a, 9b, 9c). The correlation of the simulated and the observed data is good for the
 325 magnetic field (Figure 10a), very good for the ion plasma moments and the calculated
 326 density (Figure 10c, 10e, 10g). The timeshift of the magnetic field is within five min-
 327 utes mostly (Figure 10b) however the timeshift of the ion plasma moments is scattered
 328 (Figure 10d, 10f). The timeshift of the calculated EFW density seems to be more ac-
 329 curate (Figure 10h). Generally, the GUMICS–4 is less accurate in the magnetosheath.
 330 **The modelled magnetic field is closer to the observations than the modelled**
 331 **plasma parameters are.** The calculated empirical EFW density (n_{EFW}) fits better
 332 than the CIS HIA density (n_{CIS}).

333 **3.3 Magnetosphere**

334 To select intervals in the magnetosphere we looked for the CIS HIA **omnidirectional**
 335 ionflux **spectrum**. Where the band of the hot magnetosheath ion population (dis)appeared,
 336 the magnetosphere started/finished. The solar wind density slowly becomes zero, the mag-
 337 netic field and the solar wind density drop and reach the zero value. We left 15–30 min
 338 after/before the magnetopause transition to appoint the interval in the magnetosphere.
 339 This way we found 132 intervals in the magnetosphere (Table 3) using Cluster SC3 mea-
 340 surements. The Cluster SC3 spends considerable time in the magnetosphere (Figure 11).

341 Here we show neither any correlation calculation nor comparison plot. In the mag-
 342 netosphere the GUMICS–4 does not work well. Neither the magnetic field nor the plasma
 343 moments nor the N_{EFW} fit well. The solar wind velocity does not reach zero in the sim-
 344 ulation. Instead the solar wind enters to the night side magnetosphere. The solar wind
 345 CIS HIA ion plasma density and the calculated density from spacecraft potential increase
 346 closer to the Earth (plasmasphere). The GUMICS–4 density is low there. We calculated
 347 the dipole field in GSE using Tsyganenko geotool box [Tsyganenko, 1995] and substracted
 348 from both the observed and the simulated magnetic field B_z data. The correlation of these
 349 corrected magnetic field measurements and simulations is very low too.

350 **3.4 Bow shock, magnetopause, neutral sheet**

351 78 intervals are selected when the Cluster SC3 crossed the terrestrial bow shock
 352 once or multiple times. When the spacecraft crosses the bow shock inwards the magni-
 353 tude of the magnetic field and the solar wind density increases 4–5 times (from 5 nT or
 354 5 cm^{-3} , respectively), the solar wind speed drops from 400–600 km/s to 100–300 km/s;
 355 furthermore the narrow band on the omnidirectional Cluster CIS HIA ion spectra is widened.
 356 The Cluster measurements are 1-min averaged and the GUMICS–4 simulations has 5-
 357 min resolution hence all bow shock transitions of the virtual spacecraft are slower and
 358 smoother. Additionally, the multiple bow shock transitions are not visible in the GUMICS
 359 simulations. The code reacts slowly for such sudden changes. The magnetic signatures
 360 fit better than the calculated plasma moments. The jump of the ion plasma parameters
 361 and the derived Cluster EFW density of the simulations are shifted to the measurements.
 362 Generally, the density and the velocity of the simulations seem to be less accurate than
 363 the magnetic field of the simulations.

56 intervals are selected around magnetopause crossings [...]. When the space-
 364 craft crosses the magnetopause inward direction the magnitude of the magnetic field in-
 365 creases, the solar wind speed drops from 100–300 km/s to zero, the plasma density be-
 366 comes zero; furthermore the wide band on the omnidirectional Cluster CIS HIA ion spec-
 367 tra disappears. These changes are not that fast. The location of the magnetopause is
 368 well determined by the Cluster SC3 measurements. However, it is very difficult to iden-
 369 tify the magnetopause crossings in the simulation data. [...] The magnetopause cross-
 370 ings very often cannot be seen in the simulations. Or when the magnetopause crossings
 371 are clearly identified in both simulations and spacecraft measurements the events are shifted.
 372 The accuracy of the model is lower for the dayside magnetopause locations.

Nine intervals are chosen around Cluster SC3 neutral sheet crossings (Figure 12;
 374 Table 6). The neutral sheets location is determined using the results of the Boundary
 375 Layet Identification Code (BLIC) Project [Facsikó *et al.*, in preparation]. The BLIC code
 376 determines the neutral sheet crossing Cluster FGM magnetic field measurements using
 377 Wang and Xu [1994]’s method. When the solar wind speed is almost zero; furthermore
 378 the CIS HIA density and the EFW calculated density are almost zero too; finally the GSE
 379 Z component of the magnetic field changes is a sign of the code indicated neutral sheet
 380 crossing (Figure 20; red and blue curves). Surprisingly the neutral sheet crossings are
 381 visible very well in the GUMICS simulations (Figure 20; black curves). For five events
 382 (from nine Cluster SC3 crossings) the GUMICS–4 also provides similar smoothed pa-
 383 rameters and change of sign of the B_z component. This is a **outstanding** result because
 384 the tail in the GUMICS–4 simulations is significantly smaller than the observed real-
 385 ity [Gordeev *et al.*, 2013; Facsikó *et al.*, 2016]; furthermore the solar wind enters the tail
 386 in MHD simulations generally [Kallio and Facsikó, 2015].

388 4 Discussion

The agreement of the solar wind B_z , V_x and n_{EFW} with the similar GUMICS sim-
 389 ulation parameters is very good (Figure 4a, 4b, 4c, blue). The agreement of the n_{CIS}
 390 is worse (Figure 4c, red). It was expected because the n_{EFW} depends on the spacecraft
 391 potential provided by the EFW instrument. However, the CIS instrument has many modes
 392 for measuring the plasma parameters and it needs periodical calibration too. The cor-
 393 relation of the solar wind V_x , n_{CIS} and n_{EFW} with the similar GUMICS simulation pa-
 394 rameters is greater than 0.9 (Figure 5c, 5e, 5g). The correlation of the B_z is also greater

than 0.8 (Figure 5a). Both numbers prove very high correlation. The inbound wall of
 the GUMICS–4 code is at $32 R_E$ [Janhunen et al., 2012], the nose of the terrestrial bow
 shock is at about $20 R_E$. If the solar wind speed is 400 km/s, then this spatial distance
 means less than 5 minutes delay, so it should not be visible. 80% of the intervals sup-
 port this theory but 20 % not. In these cases the one-minute resolution B_z , n_{CIS} or the
 n_{EFW} parameters have a sudden jump or variation that the simulation cannot follow,
 or the resolution of the simulation data (5 minutes) is too small to see these variations.
 Therefore, the correlation calculation is not accurate in these cases. Previously the OMNI
 data was compared to the Cluster data and the Cluster measurements were compared
 to the GUMICS–4 [Facsikó et al., 2016]. The comparison suggests that the GUMICS–4
 results should be similar with the OMNI data. Furthermore, we calculate correlation func-
 tions in the solar wind, where there is no significant perturbation of the input param-
 eters in the simulation box. Therefore, we get an expected result after comparing the
 two different correlation calculations.

In the magnetosheath we get worse agreement with the GUMICS simulation data
 (Figure 9a, 9b, 9c). However, it just means a larger uncertainty of the scattered plot.
 The general reason of this larger uncertainty seems to be the larger number of points.
 The slowed down solar wind shows strong turbulence. This phenomena explains the higher
 variations of the B_z magnetic field on Figure 9a. The solar wind V_x , n_{CIS} and n_{EFW}
 agree better than the magnetic field component (Figure 9b, 9c). Here there is no devi-
 ation between the densities derived in different ways (n_{CIS} and n_{EFW}) on Figure 9c.
 Figure 10 seems to contradict these statements above. The larger uncertainty of the B_z
 is visible on Figure 10a. However, that correlation is still good on Figure 10b. The other
 parameters have larger (> 0.9) correlation on Figure 10c, 10e, 10g. However, the time
 shifts on Figure 10d, 10f, 10h seem to be worse. Actually here the time shifts are worse
 because the shape of the time series in the magnetosheath looks very similar. Hence, the
 correlation calculation provides larger time shifts for the ion plasma parameters and the
 n_{EFW} .

In the magnetosphere the GUMICS–4 does not work well. The GUMICS–4 uses
 a tilted dipole to describe the terrestrial magnetic field [Janhunen et al., 2012]. After re-
 moving the magnetic dipole from the magnetic field measurements of the Cluster SC3
 and the simulation we get very low correlations and unacceptable time shifts (not shown).
 In the inner magnetosphere the tilted dipole is an insufficient description. However, the

429 plasma momentums and the n_{EFW} do not fit either. The MHD approach lost its validity
 430 in the inner magnetosphere domain therefore the V_x and the n of the simulations do
 431 not agree to the V_x , the n_{CIS} and the n_{EFW} measured by the Cluster SC3. Within the
 432 3.7 R_E domain another model is necessary that contains more physics as you can see it
 433 in other global MHD codes [Lyon *et al.*, 2004; Raeder *et al.*, 2008; Powell *et al.*, 1999;
 434 Tóth *et al.*, 2012]. This result explains the limited accuracy of the cross polar cap po-
 435 tential (CPCP) and geomagnetic indices of the GUMICS simulations [Juusola *et al.*, 2014].
 436 The CPCP had good agreement of GUMICS simulations and spacecraft measurements
 437 therefore this quantity could be used for capable and relevant simulation studies [Lakka
 438 *et al.*, 2018a]. Haiducek *et al.* [2017] also made a comparison study of the geomagnetic
 439 indices and the CPCP. The Space Weather Modelling Framework (SWMF) was tested.
 440 When the inner magnetosphere model was switched off in the simulation only the com-
 441 parison of the simulated and observed CPCP was good. Therefore, the reason of the dis-
 442 crepancy of the geomagnetic indices in the GUMICS simulations must be the missing
 443 inner magnetosphere model.

444 The reason of the disagreement of the simulation results and the measurements could
 445 be the code or the bad input parameters. During the 1-year run the distributions of the
 446 OMNI solar wind magnetic field B_x , B_y , B_z components (Figure 13a, 13b, 13c); solar
 447 wind velocity V_x , V_y V_z components (Figure 13d, 13e, 13f) and the solar wind P dynamic
 448 pressure are calculated (Figure 13g) from January 29, 2002 to February 2, 2003 in GSE
 449 reference frame. The intervals when the GUMICS–4 simulations and the Cluster SC3
 450 measurements disagreed are collected for intervals in the solar wind (Table 4) and the
 451 magnetosheath (Table 5). The averaged shifted OMNI parameters of the poorly agree-
 452 ing intervals from the Tables 4 and 5 are saved. The distributions of the OMNI param-
 453 eters belonging to the bad simulation results are calculated for the solar wind region (Fig-
 454 ure 14, 15 and 16) and in the magnetosheath (Figure 17, 18 and 19). In the solar wind
 455 the distributions of the OMNI B_x , B_y and B_z can be compared on Figure 13a and Fig-
 456 ure 14a, 14d, 14g, 14j; Figure 13b and Figure 14b, 14e, 14h, 14k; furthermore on Fig-
 457 ure 13c and Figure 14c, 14f, 14i, 14l. When the V_x disagrees in simulations and measure-
 458 ments on Figure 14d, 14e, 14f the distributions of the OMNI B_x , B_y and B_z are simi-
 459 lar to the distributions of the OMNI B_x , B_y and B_z on Figure 13a, 13b and 13c. When
 460 the n_{CIS} disagrees in simulations and measurements on Figure 14g, 14h, 14i the distri-
 461 butions of the OMNI B_x , B_y and B_z are similar to the distributions of the OMNI B_x ,

462 B_y and B_z on Figure 13a, 13b and 13c. When the n_{EFW} disagrees on Figure 14j, 14k, 14l
 463 the distributions of the OMNI B_x , B_y and B_z are similar to the distributions of the OMNI
 464 B_x , B_y and B_z on Figure 13a, 13b and 13c. The distributions do not agree perfectly be-
 465 cause in Table 4 the number of the poorly correlated intervals is only 6, 12 and 9 for the
 466 V_x , the n_{CIS} and n_{CIS} components, respectively. When the B_z disagrees in simulations
 467 and measurements on Figure 14a, 14b, 14c the distributions of the OMNI B_x , B_y and
 468 B_z are not similar to the distributions of the OMNI B_x , B_y and B_z on Figure 13a, 13b
 469 and 13c. The values of the OMNI B_x , B_y and B_z are not peculiar in the solar wind. The
 470 reason of these strange spikes is that there is only one poorly correlated interval for the
 471 B_z in the solar wind according to Table 4. In the solar wind the distributions of the OMNI
 472 V_x , V_y and V_z can be compared on Figure 13d and Figure 15a, 15d, 15g, 15j; Figure 13e
 473 and Figure 15b, 15e, 15h, 15k; furthermore on Figure 13f and Figure 15c, 15f, 15i, 15l.
 474 When the V_x disagrees in simulations and measurements on Figure 15d, 15e, 15f the dis-
 475 tributions of the OMNI V_x , V_y and V_z are similar to the distributions of the OMNI V_x ,
 476 V_y and V_z on Figure 13d, 13e and 13f. When the n_{CIS} disagrees on Figure 15g, 15h, 15i
 477 the distributions of the OMNI V_x , V_y and V_z are similar to the distributions of the OMNI
 478 V_x , V_y and V_z on Figure 13d, 13e and 13f. When the n_{EFW} disagrees in simulations and
 479 measurements on Figure 15j, 15k, 15l the distributions of the OMNI V_x , V_y and V_z are
 480 similar to the distributions of the OMNI V_x , V_y and V_z on Figure 13d, 13e and 13f. The
 481 distributions do not agree perfectly because in Table 4 the number of the poorly corre-
 482 lated intervals is only 6, 12 and 9 for the V_x , the n_{CIS} and n_{CIS} components, respec-
 483 tively. When the B_z disagrees on Figure 15a, 15b, 15c the distributions of the OMNI V_x ,
 484 V_y and V_z are not similar to the distributions of the OMNI V_x , V_y and V_z on Figure 13d, 13e
 485 and 13f. The values of the OMNI V_x , V_y and V_z are not peculiar in the solar wind. The
 486 reason of these strange spikes is that there is only one poorly correlated interval for the
 487 B_z in the solar wind according to Table 4. In the solar wind the distributions of the OMNI
 488 P can be compared on Figure 13g and Figure 16a, 16b, 16c, 16d. When the V_x disagrees
 489 in simulations and measurements on Figure 16b the distribution of the OMNI P is sim-
 490 ilar to the distributions of the OMNI P on Figure 13g. When the n_{CIS} disagrees in sim-
 491 ulations and measurements on Figure 16c the distribution of the OMNI P is similar to
 492 the distributions of the OMNI P on Figure 13g. When the n_{EFW} disagrees in simula-
 493 tions and measurements on Figure 16d the distribution of the OMNI P is similar to the
 494 distributions of the OMNI P on Figure 13g. The distributions do not agree perfectly be-

cause in Table 4 the number of the poorly correlated intervals is only 6, 12 and 9 for the V_x , the n_{CIS} and n_{CIS} components, respectively. When the B_z disagrees on Figure 16a the distribution of the OMNI P is not similar to the distribution of the OMNI P on Figure 13g. The values of the OMNI P are not peculiar in the solar wind. The reason of these strange spike is that there is only one poorly correlated interval for the B_z in the solar wind according to Table 4. In the magnetosheath the distributions of the OMNI B_x , B_y and B_z can be compared on Figure 13a and Figure 17a, 17d, 17g, 17j; Figure 13b and Figure 17b, 17e, 17h, 17k; furthermore on Figure 13c and Figure 17c, 17f, 17i, 17l. When the B_z disagrees in simulations and measurements on Figure 17a, 17b, 17c the distributions of the OMNI B_x , B_y and B_z are similar to the distributions of the OMNI B_x , B_y and B_z on Figure 13a, 13b and 13c. When the V_x disagrees in simulations and measurements on Figure 17d, 17e, 17f the distributions of the OMNI B_x , B_y and B_z are similar to the distributions of the OMNI B_x , B_y and B_z on Figure 13a, 13b and 13c. When the n_{CIS} disagrees in simulations and measurements on Figure 17g, 17h, 17i the distributions of the OMNI B_x , B_y and B_z are similar to the distributions of the OMNI B_x , B_y and B_z on Figure 13a, 13b and 13c. When the n_{EFW} disagrees on Figure 17j, 17k, 17l the distributions of the OMNI B_x , B_y and B_z are similar to the distributions of the OMNI B_x , B_y and B_z on Figure 13a, 13b and 13c. The distributions agree quite well because in Table 5 the number of the poorly correlated intervals 18, 50, 33 and 30 for the B_z , the V_x , the n_{CIS} and n_{CIS} components, respectively. The number of cases are higher and the values of the OMNI B_x , B_y and B_z are not peculiar in the magnetosheath. In the magnetosheath the distributions of the OMNI V_x , V_y and V_z can be compared on Figure 13d and Figure 18a, 18d, 18g, 18j; Figure 13e and Figure 18b, 18e, 18h, 18k; furthermore on Figure 13f and Figure 18c, 18f, 18i, 18l. When the B_z disagrees on Figure 18a, 18b, 18c the distributions of the OMNI V_x , V_y and V_z are similar to the distributions of the OMNI V_x , V_y and V_z on Figure 13d, 13e and 13f. When the V_x disagrees in simulations and measurements on Figure 18d, 18e, 18f the distributions of the OMNI V_x , V_y and V_z are similar to the distributions of the OMNI V_x , V_y and V_z on Figure 13d, 13e and 13f. When the n_{CIS} disagrees on Figure 18g, 18h, 18i the distributions of the OMNI V_x , V_y and V_z are similar to the distributions of the OMNI V_x , V_y and V_z on Figure 13d, 13e and 13f. When the n_{EFW} disagrees in simulations and measurements on Figure 18j, 18k, 18l the distributions of the OMNI V_x , V_y and V_z are similar to the distributions of the OMNI V_x , V_y and V_z on Figure 13d, 13e and 13f. The distributions agree quite well because in

528 Table 5 the number of the poorly correlated intervals 18, 50, 33 and 30 for the B_z , the
 529 V_x , the n_{CIS} and n_{CIS} components, respectively. The number of cases are higher and
 530 the values of the OMNI V_x , V_y and V_z are not peculiar in the magnetosheath. In the mag-
 531 netosheath the distributions of the OMNI P can be compared on Figure 13g and Fig-
 532 ure 19a, 19b, 19c, 19d. When the B_z disagrees on Figure 19a the distribution of the OMNI
 533 P is similar to the distribution of the OMNI P on Figure 13g. When the V_x disagrees
 534 in simulations and measurements on Figure 19b the distribution of the OMNI P is sim-
 535 ilar to the distributions of the OMNI P on Figure 13g. When the n_{CIS} disagrees in sim-
 536 ulations and measurements on Figure 19c the distribution of the OMNI P is similar to
 537 the distributions of the OMNI P on Figure 13g. When the n_{EFW} disagrees in simula-
 538 tions and measurements on Figure 19d the distribution of the OMNI P is similar to the
 539 distributions of the OMNI P on Figure 13g. The distributions do not agree perfectly be-
 540 cause in Table 5 the number of the poorly correlated intervals is only 6, 12 and 9 for the
 541 V_x , the n_{CIS} and n_{CIS} components, respectively. The distributions agree quite well be-
 542 cause in Table 5 the number of the poorly correlated intervals 18, 50, 33 and 30 for the
 543 B_z , the V_x , the n_{CIS} and n_{CIS} components, respectively. The number of cases are higher
 544 and the values of the OMNI P are not peculiar in the magnetosheath. The inaccuracy
 545 of the GUMICS-4 simulations does not depend on the OMNI parameters in the solar wind
 546 and magnetosheath regions. The same study does not need to be done for the magne-
 547 tosphere because the deviance of the measurements and the simulations is so large that
 548 it cannot be caused by the wrong OMNI solar wind parameters.

549 The bow shock positions agree in the GUMICS simulations and the Cluster SC3
 550 measurements. However, the magnetopause locations do not fit as good as the bow shock
 551 in simulations and observations. In simulations the location of the magnetopause is de-
 552 termined by **the downwind extension of the solar wind stagnation streamline**
 553 (**so-called fluopause**), **the maximum of the GSE Y component of the currents**
 554 density or particle density gradients [Siscoe *et al.*, 2001; García and Hughes, 2007; Gordeev
 555 *et al.*, 2013, see references therein]. In this paper the previously saved simulation param-
 556 eters along the virtual Cluster SC3 orbit are analysed. Therefore, the above mentioned
 557 methods cannot be applied. The reason of the inaccuracy of the magnetopause positions
 558 in the simulations must be the missing inner magnetosphere and ring current module.
 559 This discrepancy of the magnetopause location agrees with the results of Gordeev *et al.*
 560 [2013] and Facskó *et al.* [2016]. Gordeev *et al.* [2013] compared synthetic GUMICS runs

561 with empirical formula of the magnetopause locations. *Facskó et al.* [2016] used OMNI
 562 solar wind data as input and got the same result as *Gordeev et al.* [2013] and this pa-
 563 per. Surprisingly the neutral sheets are visible in both simulations and observations (Fig-
 564 ure 20, Table 6). This experience is exceptional because the night side magnetosphere
 565 of the GUMICS–4 simulations is small and twisted [*Gordeev et al.*, 2013; *Facskó et al.*,
 566 2016]. However, in these cases the IMF has no large B_y component. From *Facskó et al.*
 567 [2016] we know that the GUMICS has normal long tail (or night side magnetosphere)
 568 if the B_y is small.

569 5 Summary and conclusions

570 Based on the previously created 1-year long GUMICS–4 run global MHD simu-
 571 lation results are compared with Cluster SC3 magnetic field, solar wind velocity and den-
 572 sity measurements along the spacecraft orbit. Intervals are selected when the Cluster SC3
 573 and the virtual space probe are situated in the solar wind, magnetosheath and the mag-
 574 netosphere and their correlation are calculated. Bow shock, magnetopause and neutral
 575 sheet crossings are selected and their visibility and relative position are compared. We
 576 achieved the following results:

- 577 1. In the solar wind the agreement of the B_z , the V_x and the n_{EFW} is very good, fur-
 578 thermore the agreement of the n_{CIS} is also good.
- 579 2. In the magnetosheath the agreement of the magnetic field component, the ion plasma
 580 moments and the calculated empirical density is a bit worse than in the solar wind.
 581 The V_x , the n_{EFW} and the n_{CIS} fits better than the B_z component in the mag-
 582 netosheath. Their agreement is still good. The reason of the deviation is the tur-
 583 bulent behavior of the slowed down and termalised turbulent solar wind.
- 584 3. In neither the dayside nor the nightside magnetosphere can the GUMICS–4 pro-
 585 vide realistic results. The simulation outputs and the spacecraft measurement dis-
 586 agree in this region. The reason of this deviation must be the missing coupled in-
 587 ner magnetosphere model. The applied tilted dipole approach is not satisfactory
 588 in the magnetosphere at all.
- 589 4. The GUMICS–4 code causes the deviations between the simulations and the space-
 590 craft measurements because the upstream solar wind conditions seem to be nor-
 591 mal when the disagreement of the different kinds of time series is large.

592 5. The position of the bow shock and the neutral sheet agrees well in the simulations
 593 and the Cluster SC3 magnetic field, ion plasma moments and derived electron den-
 594 sity measurements in this study. The position of the magnetopause does not fit
 595 that well. The reason of this latest discrepancy must be the missing coupled in-
 596 ner magnetosphere model too.

597 The GUMICS–4 has incredible scientific and strategic importance for the European Space
 598 Weather and Scientific community. This code developed in the Finnish Meteorological
 599 Institute is the most developed and tested, widely used tool for modelling the cosmic en-
 600 viroment of the Earth in the old continent. Since the 1-year run was made some bugs
 601 of the code were fixed and the parallel version (the GUMICS–5) was developed (Honko-
 602 nen, private communication) however the parallel GUMICS is not been available on the
 603 CCMC or the VSWMC yet. We believe that the scientific community will have access
 604 to the new version and an inner magnetosphere model will be two way coupled to the
 605 existing configuration of the simulation tool.

606 Acknowledgments

607 The OMNI data were obtained from the GSFC/SPDF OMNIWeb interface at <http://omniweb.gsfc.nasa.gov>.
 608 The authors thank the FGM Team (PI: Chris Carr), the CIS Team (PI: Iannis Dandouras),
 609 the WHISPER Team (PI: Jean-Louis Rauch), the EFW Team (PI: Mats Andre) and the
 610 Cluster Science Archive for providing FGM magnetic field, CIS HIA ion plasma and WHIS-
 611 PER electron density measurements. Data analysis was partly done with the QSAS sci-
 612 ence analysis system provided by the United Kingdom Cluster Science Centre (Impe-
 613 rial College London and Queen Mary, University of London) supported by the Science
 614 and Technology Facilities Council (STFC). Eija Tanskanen acknowledges financial sup-
 615 port from the Academy of Finland for the ReSoLVE Centre of Excellence (project No. 272157).
 616 Gábor Facskó thanks Anna-Mária Vígh for improving the English of the paper. The au-
 617 thors thank Pekka Janhunen for developing the GUMICS–4 code; furthermore Minna
 618 Palmroth and Zoltán Vörös for the useful discussions. The work of Gábor Facskó was
 619 supported by mission science funding for the Van Allen Probes mission, the American
 620 Geophysical Union and the HAS Research Centre for Astronomy and Earth Sciences,
 621 Sopron, Hungary. For further use of the year run data, [...] **request the authors or**
 622 use the archive of the Community Coordinated Modelling Center (<https://ccmc.gsfc.nasa.gov/publications/posted>)

623

624 References

- 625 Balogh, A., M. W. Dunlop, S. W. H. Cowley, D. J. Southwood, J. G. Thomlinson,
 626 K. H. Glassmeier, G. Musmann, H. Luhr, S. Buchert, M. H. Acuna, D. H. Fair-
 627 field, J. A. Slavin, W. Riedler, K. Schwingenschuh, and M. G. Kivelson (1997),
 628 The Cluster Magnetic Field Investigation, *Space Science Reviews*, 79, 65–91, doi:
 629 10.1023/A:1004970907748.
- 630 Balogh, A., C. M. Carr, M. H. Acuña, M. W. Dunlop, T. J. Beek, P. Brown,
 631 K. Fornaçon, E. Georgescu, K. Glassmeier, J. Harris, G. Musmann, T. Oddy, and
 632 K. Schwingenschuh (2001), The Cluster Magnetic Field Investigation: overview of
 633 in-flight performance and initial results, *Annales Geophysicae*, 19, 1207–1217.
- 634 Bartels, J., N. H. Heck, and H. F. Johnston (1939), The three-hour-range index mea-
 635 suring geomagnetic activity, *Terrestrial Magnetism and Atmospheric Electricity*
 636 (*Journal of Geophysical Research*), 44, 411, doi:10.1029/TE044i004p00411.
- 637 Blagau, A., I. Dandouras, A. Barthe, S. Brunato, G. Facskó, and V. Constanti-
 638 nescu (2013), In-flight calibration of Hot Ion Analyser onboard Cluster, *Geo-
 639 scientific Instrumentation, Methods and Data Systems Discussions*, 3, 407–435,
 640 doi:10.5194/gid-3-407-2013.
- 641 Blagau, A., I. Dandouras, A. Barthe, S. Brunato, G. Facskó, and V. Constantinescu
 642 (2014), In-flight calibration of the Hot Ion Analyser on board Cluster, *Geoscientific
 643 Instrumentation, Methods and Data Systems*, 3, 49–58, doi:10.5194/gi-3-49-
 644 2014.
- 645 Chittenden, J. P., S. V. Lebedev, C. A. Jennings, S. N. Bland , and A. Ciardi
 646 (2004), X-ray generation mechanisms in three-dimensional simulations of wire
 647 array Z-pinches, *Plasma Physics and Controlled Fusion*, 46(12B), B457–B476,
 648 doi:10.1088/0741-3335/46/12B/039.
- 649 Ciardi, A., S. V. Lebedev, A. Frank, E. G. Blackman, J. P. Chittenden, C. J. Jen-
 650 nings, D. J. Ampleford, S. N. Bland, S. C. Bott, J. Rapley, G. N. Hall, F. A.
 651 Suzuki-Vidal, A. Marocchino, T. Lery, and C. Stehle (2007), The evolution of
 652 magnetic tower jets in the laboratory, *Physics of Plasmas*, 14(5), 056,501–056,501,
 653 doi:10.1063/1.2436479.
- 654 Credland, J., G. Mecke, and J. Ellwood (1997), The Cluster Mission: ESA'S
 655 Spacefleet to the Magnetosphere, *Space Science Reviews*, 79, 33–64, doi:
 656 10.1023/A:1004914822769.

- 657 Davis, T. N., and M. Sugiura (1966), Auroral electrojet activity index AE and its
658 universal time variations, *Journal of Geophysical Research*, *71*, 785–801, doi:
659 10.1029/JZ071i003p00785.
- 660 Décréau, P. M. E., P. Fergeau, V. Krasnoselskikh, E. Le Guiriec, M. Lévéque,
661 P. Martin, O. Randriamboarison, J. L. Rauch, F. X. Sené, H. C. Séran, J. G.
662 Trotignon, P. Canu, N. Cornilleau, H. de Féraudy, H. Alleyne, K. Yearby, P. B.
663 Mögensen, G. Gustafsson, M. André, D. C. Gurnett, F. Darrouzet, J. Lemaire,
664 C. C. Harvey, P. Travnicek, and Whisper Experimenters Group (2001), Early re-
665 sults from the Whisper instrument on Cluster: an overview, *Annales Geophysicae*,
666 *19*, 1241–1258, doi:10.5194/angeo-19-1241-2001.
- 667 Escoubet, C. P., M. Fehringer, and M. Goldstein (2001), Introduction The Cluster
668 mission, *Annales Geophysicae*, *19*, 1197–1200, doi:10.5194/angeo-19-1197-2001.
- 669 Facskó, G., I. Honkonen, T. Živković, L. Palin, E. Kallio, K. Ågren, H. Opgenoorth,
670 E. I. Tanskanen, and S. Milan (2016), One year in the Earth's magnetosphere: A
671 global MHD simulation and spacecraft measurements, *Space Weather*, *14*, 351–
672 367, doi:10.1002/2015SW001355.
- 673 Facskó, G., T. B. Balogh, E. I. Anekallu, C. R. and Tanskanen, P. Peitso, L. Degener,
674 M. Kangwa, T. Laitinen, and S. Laakso, H. Burley (in preparation), Bow shock
675 identification in cluster measurements, *Space Weather*.
- 676 Fazakerley, A. N., A. D. Lahiff, R. J. Wilson, I. Rozum, C. Anekallu, M. West, and
677 H. Bacai (2010a), PEACE Data in the Cluster Active Archive, *Astrophysics and
678 Space Science Proceedings*, *11*, 129–144, doi:10.1007/978-90-481-3499-1_8.
- 679 Fazakerley, A. N., A. D. Lahiff, I. Rozum, D. Kataria, H. Bacai, C. Anekallu,
680 M. West, and A. Åsnes (2010b), Cluster-PEACE In-flight Calibration Status,
681 *Astrophysics and Space Science Proceedings*, *11*, 281–299, doi:10.1007/978-90-481-
682 3499-1_19.
- 683 García, K. S., and W. J. Hughes (2007), Finding the Lyon-Fedder-Mobarry mag-
684 netopause: A statistical perspective, *Journal of Geophysical Research (Space
685 Physics)*, *112*(A6), A06229, doi:10.1029/2006JA012039.
- 686 Gordeev, E., G. Facskó, V. Sergeev, I. Honkonen, M. Palmroth, P. Janhunen, and
687 S. Milan (2013), Verification of the GUMICS-4 global MHD code using empirical
688 relationships, *Journal of Geophysical Research (Space Physics)*, *118*, 3138–3146,
689 doi:10.1002/jgra.50359.

- 690 Greenwald, R. A., K. B. Baker, J. R. Dudeney, M. Pinnock, T. B. Jones, E. C.
691 Thomas, J.-P. Villain, J.-C. Cerisier, C. Senior, C. Hanuise, R. D. Hunsucker,
692 G. Sofko, J. Koehler, E. Nielsen, R. Pellinen, A. D. M. Walker, N. Sato,
693 and H. Yamagishi (1995), Darn/Superdarn: A Global View of the Dynam-
694 ics of High-Latitude Convection, *Space Science Reviews*, *71*, 761–796, doi:
695 10.1007/BF00751350.
- 696 Guild, T. B., H. E. Spence, E. L. Kepko, V. Merkin, J. G. Lyon, M. Wiltberger, and
697 C. C. Goodrich (2008a), Geotail and LFM comparisons of plasma sheet clima-
698 tology: 1. Average values, *Journal of Geophysical Research (Space Physics)*, *113*,
699 A04216, doi:10.1029/2007JA012611.
- 700 Guild, T. B., H. E. Spence, E. L. Kepko, V. Merkin, J. G. Lyon, M. Wiltberger, and
701 C. C. Goodrich (2008b), Geotail and LFM comparisons of plasma sheet climatol-
702 ogy: 2. Flow variability, *Journal of Geophysical Research (Space Physics)*, *113*,
703 A04217, doi:10.1029/2007JA012613.
- 704 Gustafsson, G., R. Bostrom, B. Holback, G. Holmgren, A. Lundgren, K. Stasiewicz,
705 L. Ahlen, F. S. Mozer, D. Pankow, P. Harvey, P. Berg, R. Ulrich, A. Pedersen,
706 R. Schmidt, A. Butler, A. W. C. Fransen, D. Klinge, M. Thomsen, C.-G. Faltham-
707 mar, P.-A. Lindqvist, S. Christenson, J. Holtet, B. Lybekk, T. A. Sten, P. Tan-
708 skanen, K. Lappalainen, and J. Wygant (1997), The Electric Field and Wave
709 Experiment for the Cluster Mission, *Space Science Reviews*, *79*, 137–156, doi:
710 10.1023/A:1004975108657.
- 711 Gustafsson, G., M. André, T. Carozzi, A. I. Eriksson, C.-G. Fälthammar, R. Grard,
712 G. Holmgren, J. A. Holtet, N. Ivchenko, T. Karlsson, Y. Khotyaintsev, S. Klimov,
713 H. Laakso, P.-A. Lindqvist, B. Lybekk, G. Marklund, F. Mozer, K. Mursula,
714 A. Pedersen, B. Popielawska, S. Savin, K. Stasiewicz, P. Tanskanen, A. Vaivads,
715 and J.-E. Wahlund (2001), First results of electric field and density observations
716 by Cluster EFW based on initial months of operation, *Annales Geophysicae*, *19*,
717 1219–1240, doi:10.5194/angeo-19-1219-2001.
- 718 Haiducek, J. D., D. T. Welling, N. Y. Ganushkina, S. K. Morley, and D. S. Oz-
719 turk (2017), SWMF Global Magnetosphere Simulations of January 2005: Geo-
720 magnetic Indices and Cross-Polar Cap Potential, *Space Weather*, *15*, 1567–1587,
721 doi:10.1002/2017SW001695.
- 722 Iyemori, T. (1990), Storm-time magnetospheric currents inferred from mid-latitude

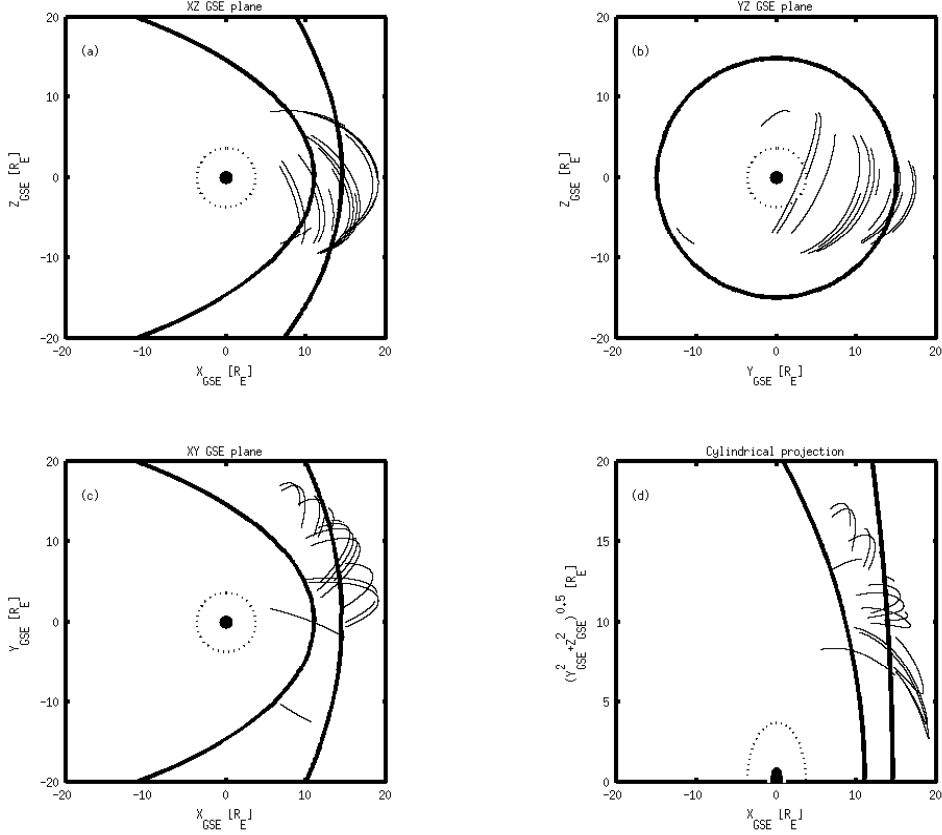
- 723 geomagnetic field variations, *Journal of Geomagnetism and Geoelectricity*, 42,
724 1249–1265, doi:10.5636/jgg.42.1249.
- 725 Janhunen, P., M. Palmroth, T. Laitinen, I. Honkonen, L. Juusola, G. Facskó, and
726 T. I. Pulkkinen (2012), The GUMICS-4 global MHD magnetosphere-ionosphere
727 coupling simulation, *Journal of Atmospheric and Solar-Terrestrial Physics*, 80,
728 48–59, doi:10.1016/j.jastp.2012.03.006.
- 729 Johnstone, A. D., C. Alsop, S. Burge, P. J. Carter, A. J. Coates, A. J. Coker, A. N.
730 Fazakerley, M. Grande, R. A. Gowen, C. Gurgiolo, B. K. Hancock, B. Narheim,
731 A. Preece, P. H. Sheather, J. D. Winningham, and R. D. Woodliffe (1997), Peace:
732 a Plasma Electron and Current Experiment, *Space Science Reviews*, 79, 351–398,
733 doi:10.1023/A:1004938001388.
- 734 Juusola, L., O. Amm, K. Kauristie, and A. Viljanen (2007), A model for estimating
735 the relation between the Hall to Pedersen conductance ratio and ground magnetic
736 data derived from CHAMP satellite statistics, *Annales Geophysicae*, 25, 721–736,
737 doi:10.5194/angeo-25-721-2007.
- 738 Juusola, L., G. Facskó, I. Honkonen, P. Janhunen, H. Vanhamäki, K. Kauristie,
739 T. V. Laitinen, S. E. Milan, M. Palmroth, E. I. Tanskanen, and A. Viljanen
740 (2014), Statistical comparison of seasonal variations in the GUMICS-4 global
741 MHD model ionosphere and measurements, *Space Weather*, 12, 582–600, doi:
742 10.1002/2014SW001082.
- 743 Kallio, E., and G. Facskó (2015), Properties of plasma near the moon in the magne-
744 totail, *Planetary and Space Science*, 115, 69–76, doi:10.1016/j.pss.2014.11.007.
- 745 Kokubun, S., T. Yamamoto, M. H. Acuña, K. Hayashi, K. Shiokawa, and H. Kawano
746 (1994), The GEOTAIL Magnetic Field Experiment., *Journal of Geomagnetism*
747 and *Geoelectricity*, 46, 7–21, doi:10.5636/jgg.46.7.
- 748 Lakka, A., T. I. Pulkkinen, A. P. Dimmock, M. Myllys, I. Honkonen, and M. Palm-
749 roth (2018a), The Cross-Polar Cap Saturation in GUMICS-4 During High Solar
750 Wind Driving, *Journal of Geophysical Research (Space Physics)*, 123, 3320–3332,
751 doi:10.1002/2017JA025054.
- 752 Lakka, A., T. I. Pulkkinen, A. P. Dimmock, E. Kilpua, M. Ala-Lahti, I. Honko-
753 nen, M. Palmroth, and Raukunen (2018b), Icme impact at earth with low and
754 typical mach number plasma characteristics, *Annales Geophysicae Discussions*,
755 <https://doi.org/10.5194/angeo-2018-81>.

- 756 Lani, A., A. Sanna, N. Villedieu, and M. Panesi (2012), COOLFluiD an Open Com-
757 putational Platform for Aerothermodynamics and Flow-Radiation Coupling, in
758 *ESA Special Publication, ESA Special Publication*, vol. 714, p. 45.
- 759 Lyon, J. G., J. A. Fedder, and C. M. Mobarry (2004), The Lyon-Fedder-Mobarry
760 (LFM) global MHD magnetospheric simulation code, *Journal of Atmospheric and*
761 *Solar-Terrestrial Physics*, 66, 1333–1350, doi:10.1016/j.jastp.2004.03.020.
- 762 Mejnertsen, L., J. P. Eastwood, J. P. Chittenden, and A. Masters (2016), Global
763 MHD simulations of Neptune's magnetosphere, *Journal of Geophysical Research*
764 (*Space Physics*), 121(8), 7497–7513, doi:10.1002/2015JA022272.
- 765 Mejnertsen, L., J. P. Eastwood, H. Hietala, S. J. Schwartz, and J. P. Chittenden
766 (2018), Global MHD Simulations of the Earth's Bow Shock Shape and Motion
767 Under Variable Solar Wind Conditions, *Journal of Geophysical Research (Space*
768 *Physics*), 123(1), 259–271, doi:10.1002/2017JA024690.
- 769 Mukai, T., S. Machida, Y. Saito, M. Hirahara, T. Terasawa, N. Kaya, T. Obara,
770 M. Ejiri, and A. Nishida (1994), The Low Energy Particle (LEP) Experiment on-
771 board the GEOTAIL Satellite., *Journal of Geomagnetism and Geoelectricity*, 46,
772 669–692, doi:10.5636/jgg.46.669.
- 773 Peredo, M., J. A. Slavin, E. Mazur, and S. A. Curtis (1995), Three-dimensional po-
774 sition and shape of the bow shock and their variation with Alfvénic, sonic and
775 magnetosonic Mach numbers and interplanetary magnetic field orientation, *Jour-*
776 *nal of Geophysical Research*, 100, 7907–7916, doi:10.1029/94JA02545.
- 777 Poedts, S., A. Kochanov, A. Lani, C. Scolini, C. Verbeke, S. Hosteaux, E. Chané,
778 H. Deconinck, N. Mihalache, F. Diet, D. Heynderickx, J. De Keyser, E. De
779 Donder, N. B. Crosby, M. Echim, L. Rodriguez, R. Vansintjan, F. Verstringe,
780 B. Mampaey, R. Horne, S. Glauert, P. Jiggens, R. Keil, A. Glover, G. Deprez, and
781 J.-P. Luntama (2020), The Virtual Space Weather Modelling Centre, *Journal of*
782 *Space Weather and Space Climate*, 10, 14, doi:10.1051/swsc/2020012.
- 783 Powell, K. G., P. L. Roe, T. J. Linde, T. I. Gombosi, and D. L. De Zeeuw (1999), A
784 Solution-Adaptive Upwind Scheme for Ideal Magnetohydrodynamics, *Journal of*
785 *Computational Physics*, 154, 284–309, doi:10.1006/jcph.1999.6299.
- 786 Raeder, J., D. Larson, W. Li, E. L. Kepko, and T. Fuller-Rowell (2008), OpenG-
787 GCM Simulations for the THEMIS Mission, *Space Science Reviews*, 141, 535–555,
788 doi:10.1007/s11214-008-9421-5.

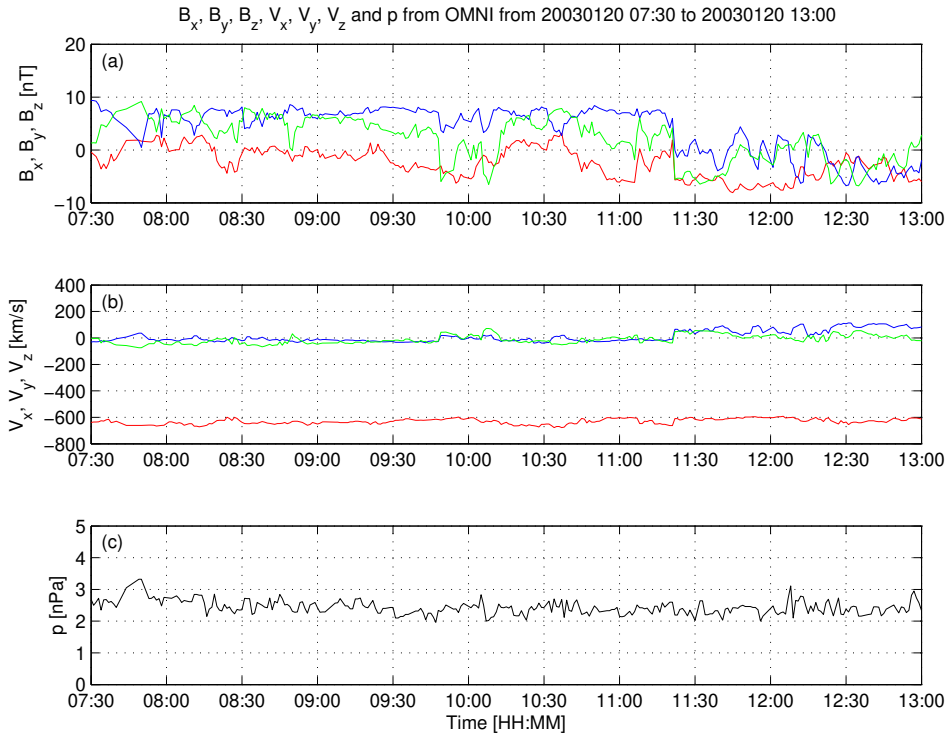
- 789 Reigber, C., H. Lühr, and P. Schwintzer (2002), CHAMP mission status, *Advances*
 790 *in Space Research*, 30, 129–134, doi:10.1016/S0273-1177(02)00276-4.
- 791 Reme, H., J. M. Bosqued, J. A. Sauvaud, A. Cros, J. Dandouras, C. Aoustin,
 792 J. Bouyssou, T. Camus, J. Cuvilo, C. Martz, J. L. Medale, H. Perrier, D. Rome-
 793 fort, J. Rouzaud, C. D'Uston, E. Möbius, K. Crocker, M. Granoff, L. M. Kistler,
 794 M. Popecki, D. Hovestadt, B. Klecker, G. Paschmann, M. Scholer, C. W. Carl-
 795 son, D. W. Curtis, R. P. Lin, J. P. McFadden, V. Formisano, E. Amata, M. B.
 796 Bavassano-Cattaneo, P. Baldetti, G. Belluci, R. Bruno, G. Chionchio, A. di Lel-
 797 lis, E. G. Shelley, A. G. Ghielmetti, W. Lennartsson, A. Korth, H. Rosenbauer,
 798 R. Lundin, S. Olsen, G. K. Parks, M. McCarthy, and H. Balsiger (1997), The
 799 Cluster Ion Spectrometry (CIS) Experiment, *Space Science Reviews*, 79, 303–350,
 800 doi:10.1023/A:1004929816409.
- 801 Rème, H., C. Aoustin, J. M. Bosqued, I. Dandouras, B. Lavraud, J. A. Sauvaud,
 802 A. Barthe, J. Bouyssou, T. Camus, O. Coeur-Joly, A. Cros, J. Cuvilo, F. Ducay,
 803 Y. Garbarowitz, J. L. Medale, E. Penou, H. Perrier, D. Romefort, J. Rouzaud,
 804 C. Vallat, D. Alcaydé, C. Jacquay, C. Mazelle, C. D'Uston, E. Möbius, L. M.
 805 Kistler, K. Crocker, M. Granoff, C. Mouikis, M. Popecki, M. Vosbury, B. Klecker,
 806 D. Hovestadt, H. Kucharek, E. Kuenneth, G. Paschmann, M. Scholer, N. Sckopke,
 807 E. Seidenschwang, C. W. Carlson, D. W. Curtis, C. Ingraham, R. P. Lin, J. P.
 808 McFadden, G. K. Parks, T. Phan, V. Formisano, E. Amata, M. B. Bavassano-
 809 Cattaneo, P. Baldetti, R. Bruno, G. Chionchio, A. di Lellis, M. F. Marcucci,
 810 G. Pallocchia, A. Korth, P. W. Daly, B. Graeve, H. Rosenbauer, V. Vasyliunas,
 811 M. McCarthy, M. Wilber, L. Eliasson, R. Lundin, S. Olsen, E. G. Shelley, S. Fuse-
 812 lier, A. G. Ghielmetti, W. Lennartsson, C. P. Escoubet, H. Balsiger, R. Friedel, J.-
 813 B. Cao, R. A. Kovrashkin, I. Papamastorakis, R. Pellat, J. Scudder, and B. Son-
 814 nerup (2001), First multispacecraft ion measurements in and near the Earth's
 815 magnetosphere with the identical Cluster ion spectrometry (CIS) experiment,
 816 *Annales Geophysicae*, 19, 1303–1354, doi:10.5194/angeo-19-1303-2001.
- 817 Ritter, P., H. Lühr, A. Viljanen, O. Amm, A. Pulkkinen, and I. Sillanpää (2004),
 818 Ionospheric currents estimated simultaneously from CHAMP satellite and IMAGE
 819 ground-based magnetic field measurements: a statistical study at auroral latitudes,
 820 *Annales Geophysicae*, 22, 417–430, doi:10.5194/angeo-22-417-2004.
- 821 Rostoker, G. (1972), Geomagnetic indices., *Reviews of Geophysics and Space*

- 822 *Physics*, **10**, 935–950, doi:10.1029/RG010i004p00935.
- 823 Siscoe, G. L., G. M. Erickson, B. U. Sonnerup, N. C. Maynard, J. A. Schoendorf,
 824 K. D. Siebert, D. R. Weimer, W. W. White, and G. R. Wilson (2001), The Mag-
 825 netospheric Fluopause, in *AGU Spring Meeting Abstracts*, vol. 2001, pp. SM52D–
 826 02.
- 827 Sofko, G. J., R. Greenwald, and W. Bristow (1995), Direct determination of large-
 828 scale magnetospheric field-aligned currents with SuperDARN, *Geophysical Re-*
 829 *search Letters*, **22**, 2041–2044, doi:10.1029/95GL01317.
- 830 Thomsen, M. F. (2004), Why K_p is such a good measure of magnetospheric convec-
 831 tion, *Space Weather*, **2**, S11004, doi:10.1029/2004SW000089.
- 832 Tóth, G., I. V. Sokolov, T. I. Gombosi, D. R. Chesney, C. R. Clauer, D. L. de
 833 Zeeuw, K. C. Hansen, K. J. Kane, W. B. Manchester, R. C. Oehmke, K. G. Pow-
 834 ell, A. J. Ridley, I. I. Roussev, Q. F. Stout, O. Volberg, R. A. Wolf, S. Sazykin,
 835 A. Chan, B. Yu, and J. Kóta (2005), Space Weather Modeling Framework: A
 836 new tool for the space science community, *Journal of Geophysical Research (Space*
 837 *Physics*), **110**, A12226, doi:10.1029/2005JA011126.
- 838 Tóth, G., B. van der Holst, I. V. Sokolov, D. L. De Zeeuw, T. I. Gombosi, F. Fang,
 839 W. B. Manchester, X. Meng, D. Najib, K. G. Powell, Q. F. Stout, A. Glo-
 840 cer, Y.-J. Ma, and M. Opher (2012), Adaptive numerical algorithms in space
 841 weather modeling, *Journal of Computational Physics*, **231**, 870–903, doi:
 842 10.1016/j.jcp.2011.02.006.
- 843 Trotignon, J. G., P. M. E. Décréau, J. L. Rauch, X. Vallières, A. Rochel,
 844 S. Kouglénou, G. Lointier, G. Facskó, P. Canu, F. Darrouzet, and A. Masson
 845 (2010), The WHISPER Relaxation Sounder and the CLUSTER Active Archive,
 846 *Astrophysics and Space Science Proceedings*, **11**, 185–208, doi:10.1007/978-90-481-
 847 3499-1_12.
- 848 Trotignon, J.-G., Vallières, and the WHISPER team (2011), Calibration report of
 849 the whisper measurements in the cluster active archive (caa), *Tech. rep.*, LPC2E
 850 CNRS, caa-est-cr-whi.
- 851 Tsyganenko, N. A. (1995), Modeling the Earth's magnetospheric magnetic field
 852 confined within a realistic magnetopause, *Journal of Geophysical Research*, **100**,
 853 5599–5612, doi:10.1029/94JA03193.
- 854 Vörös, Z., G. Facskó, M. Khodachenko, I. Honkonen, P. Janhunen, and M. Palmroth

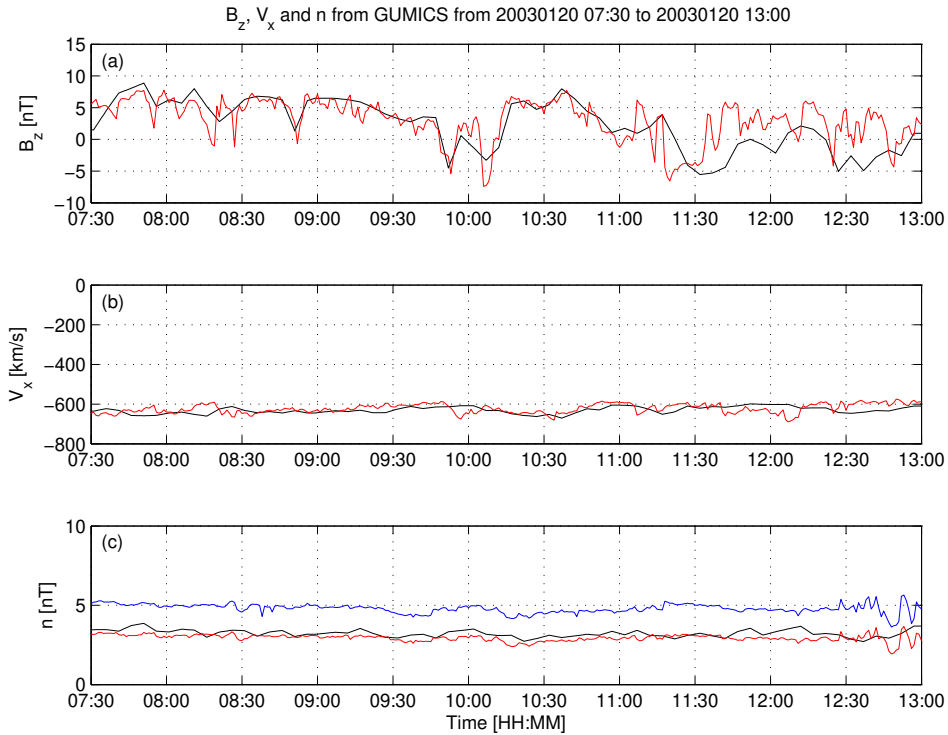
- 855 (2014), Windsock memory COnditioned RAM (CO-RAM) pressure effect: Forced
856 reconnection in the Earth's magnetotail, *Journal of Geophysical Research (Space*
857 *Physics)*, 119, 6273–6293, doi:10.1002/2014JA019857.
- 858 Wang, Z.-D., and R. L. Xu (1994), Signatures of the magnetotail neutral sheet,
859 *Geophysical Research Letters*, 21(19), 2087–2090, doi:10.1029/94GL01960.
- 860 Weimer, D. R. (2005), Improved ionospheric electrodynamic models and applica-
861 tion to calculating Joule heating rates, *Journal of Geophysical Research (Space*
862 *Physics)*, 110, A05306, doi:10.1029/2004JA010884.
- 863 Wiltberger, M., E. J. Rigler, V. Merkin, and J. G. Lyon (2017), Structure of High
864 Latitude Currents in Magnetosphere-Ionosphere Models, *Space Science Reviews*,
865 206, 575–598, doi:10.1007/s11214-016-0271-2.
- 866 Zhang, B., W. Lotko, M. J. Wiltberger, O. J. Brambles, and P. A. Damiano (2011),
867 A statistical study of magnetosphere-ionosphere coupling in the Lyon-Fedder-
868 Mobarry global MHD model, *Journal of Atmospheric and Solar-Terrestrial*
869 *Physics*, 73, 686–702, doi:10.1016/j.jastp.2010.09.027.



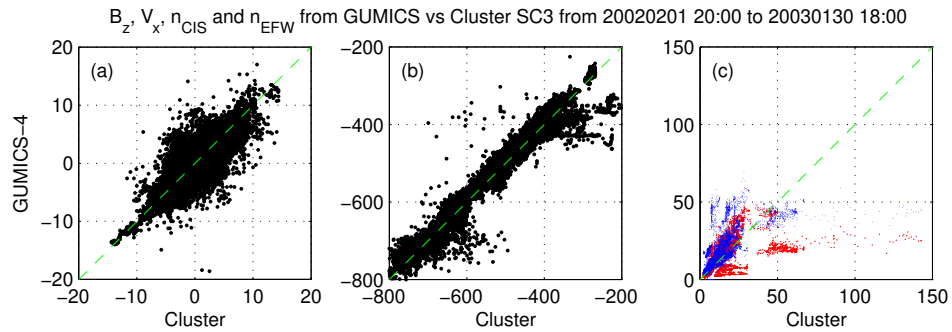
870 **Figure 1.** Cluster SC3 orbit in the solar wind in GSE system for all intervals (see Table 1).
 871 (a) XZ (b) YZ (c) XY (d) Cylindrical projection. Average bow-shock and magnetopause posi-
 872 tions are drawn on all plots using solid line [Perego *et al.*, 1995; Tsyganenko, 1995, respectively].
 873 The black dots at $3.7 R_E$ show the boundary of the GUMICS-4 inner magnetospheric domain.
 874 The black circle in the origo of all plots shows the size of the Earth.



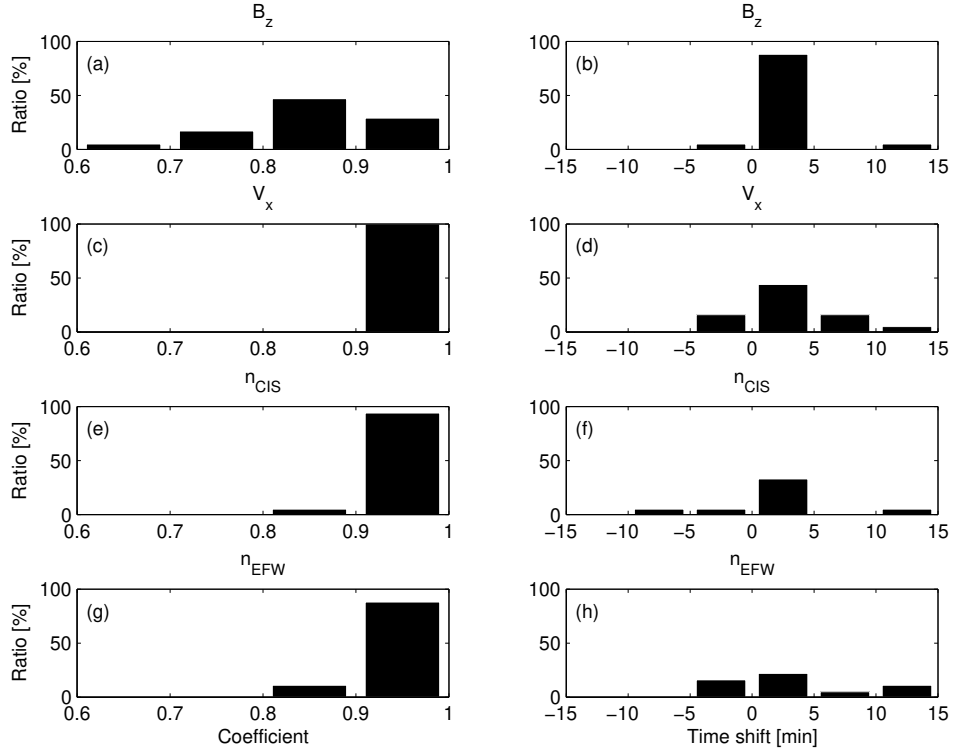
875 **Figure 2.** OMNI solar wind data in GSE system from 7:30 to 13:00 (UT) on January 20,
 876 2003. (a) Magnetic field B_x (red), B_y (green) and B_z (blue) components. (b) Solar wind velocity
 877 V_x (red), V_y (green) and V_z (blue) components. (c) The P pressure of the solar wind (black).



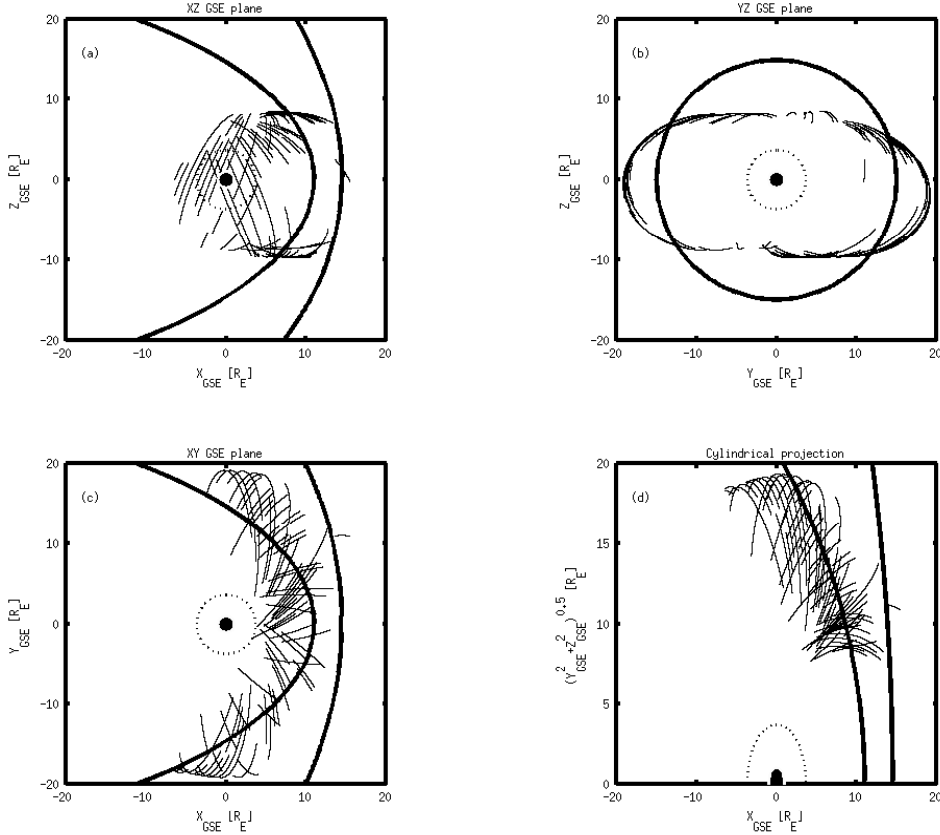
878 **Figure 3.** GUMICS-4 simulation results (black) and Cluster SC3 magnetic field Z component,
 879 ion plasma moments (red) and electron density calculated from spacecraft potential (blue) from
 880 January 20, 2003 from 7:30 to 13:00 (UT) in the solar wind in GSE system. (a) Magnetic field Z
 881 component. (b) Solar wind velocity X component (c) Solar wind density.



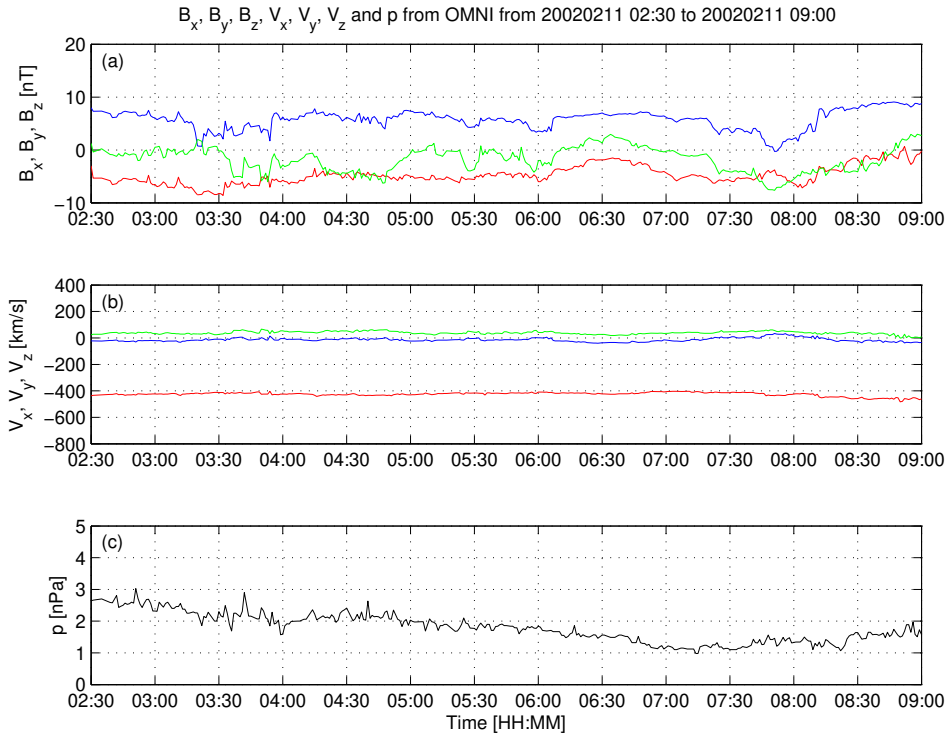
882 **Figure 4.** Scattered plots of the Cluster SC3 and GUMICS-4 simulations for all intervals in
 883 the solar wind. The dashed line is the $y=x$ line. (a) Magnetic field Z component in GSE system.
 884 (b) Solar wind velocity X component in GSE system. (c) Solar wind density measured by the
 885 CIS HIA instrument (red) and calculated from the spacecraft potential (blue).



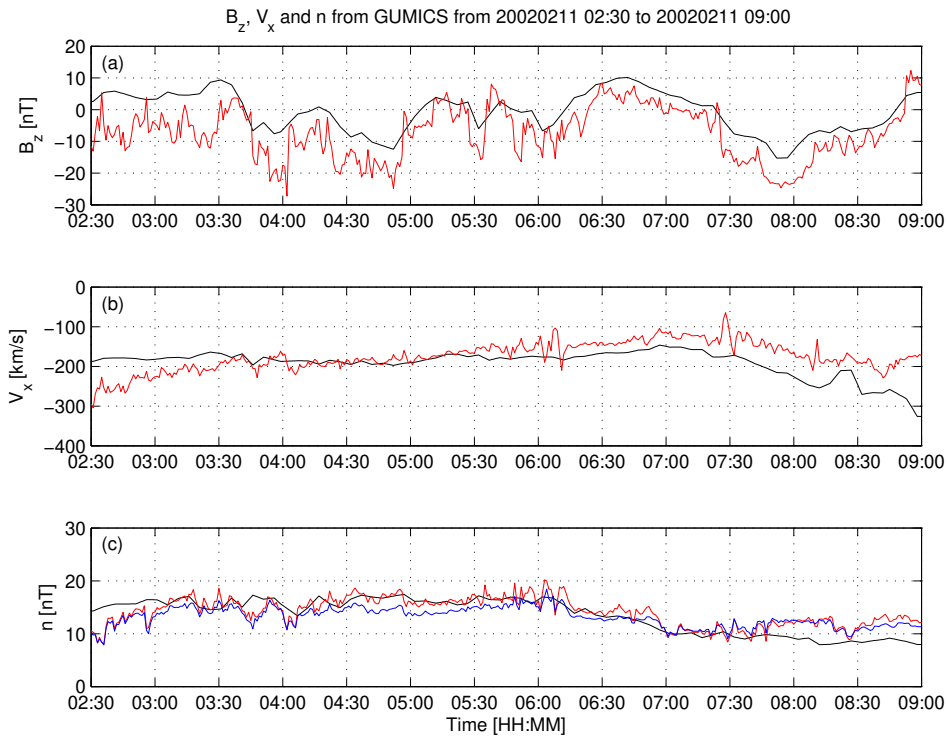
886 **Figure 5.** The distributions of the correlation coefficients (a, c, e, g) of the magnetic field Z
 887 component (B_z) in GSE system, solar wind velocity X component (V_X) in GSE system, the solar
 888 wind density measured by the CIS HIA (n_{CIS}) instrument and calculated from the spacecraft
 889 potential (n_{EFW}), respectively, for all intervals in the solar wind. The distributions of the time
 890 shifts (b, d, f, h) of the B_z , the V_X , the n_{CIS} and the n_{EFW} , respectively, for all intervals in the
 891 solar wind.



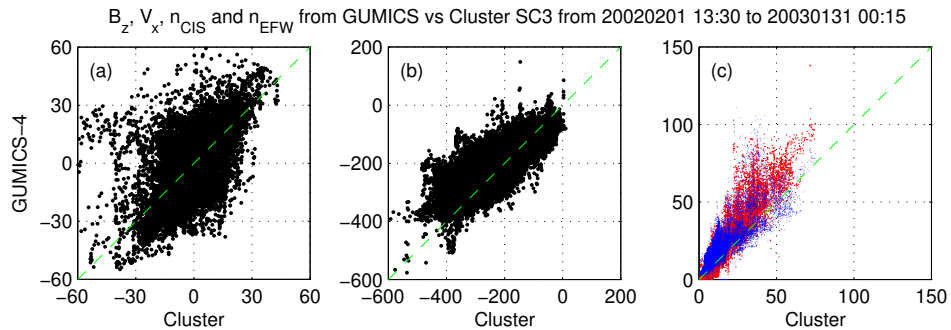
892 **Figure 6.** Cluster SC3 orbit in the magnetosheath in GSE system for all intervals (see Ta-
 893 ble 2). (a) XZ (b) YZ (c) XY (d) Cylindrical projection. Average bow-shock and magnetopause
 894 positions are drawn on all plots using solid line [Peredo *et al.*, 1995; Tsyganenko, 1995, respec-
 895 tively]. The black dots at $3.7 R_E$ show the boundary of the GUMICS-4 inner magnetospheric
 896 domain. The black circle in the origo of all plots shows the size of the Earth.



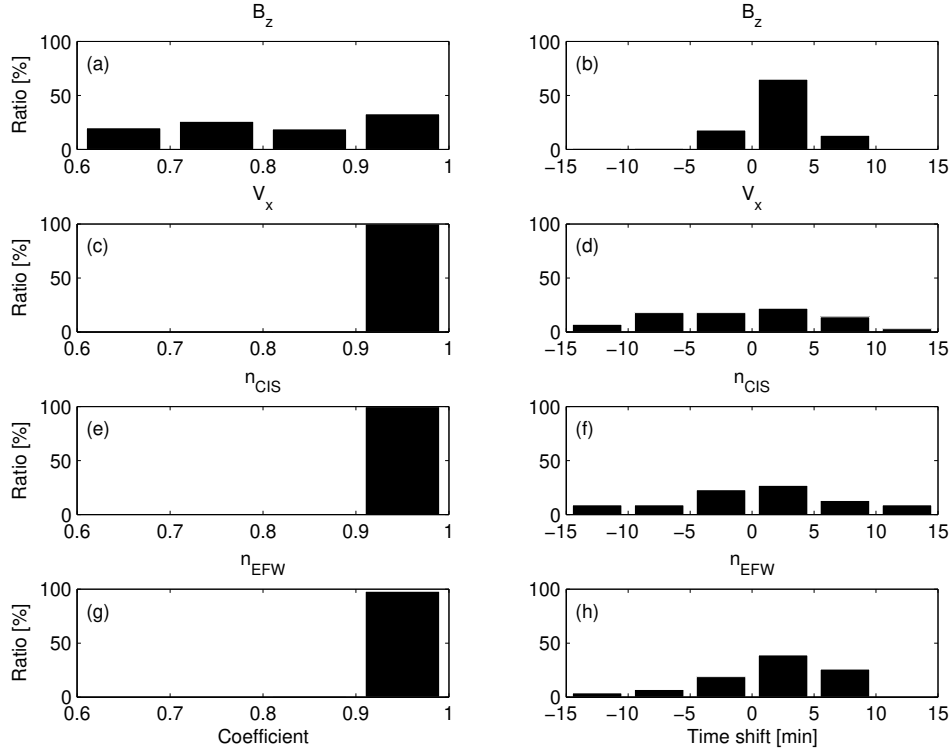
897 **Figure 7.** OMNI solar wind data in GSE system from 2:30 to 09:00 (UT) on February 11,
 898 2002. (a) Magnetic field B_x (red), B_y (green) and B_z (blue) components. (b) Solar wind velocity
 899 V_x (red), V_y (green) and V_z (blue) components. (c) The P pressure of the solar wind (black).



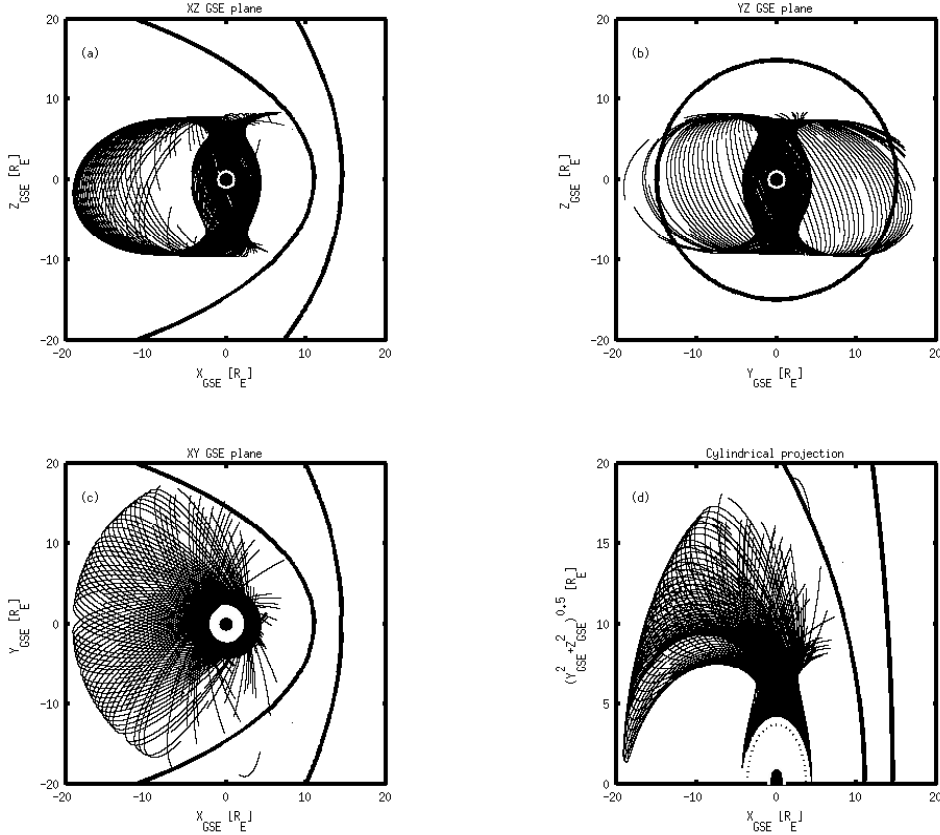
900 **Figure 8.** GUMICS-4 simulation results (black) and Cluster SC3 magnetic field Z component,
 901 ion plasma moments (red) and electron density calculated from spacecraft potential (blue) from
 902 February 11, 2002 from 2:30 to 9:00 (UT) in the magnetosheath in GSE system (a) Magnetic
 903 field Z component. (b) Solar wind velocity X component (c) Solar wind density.



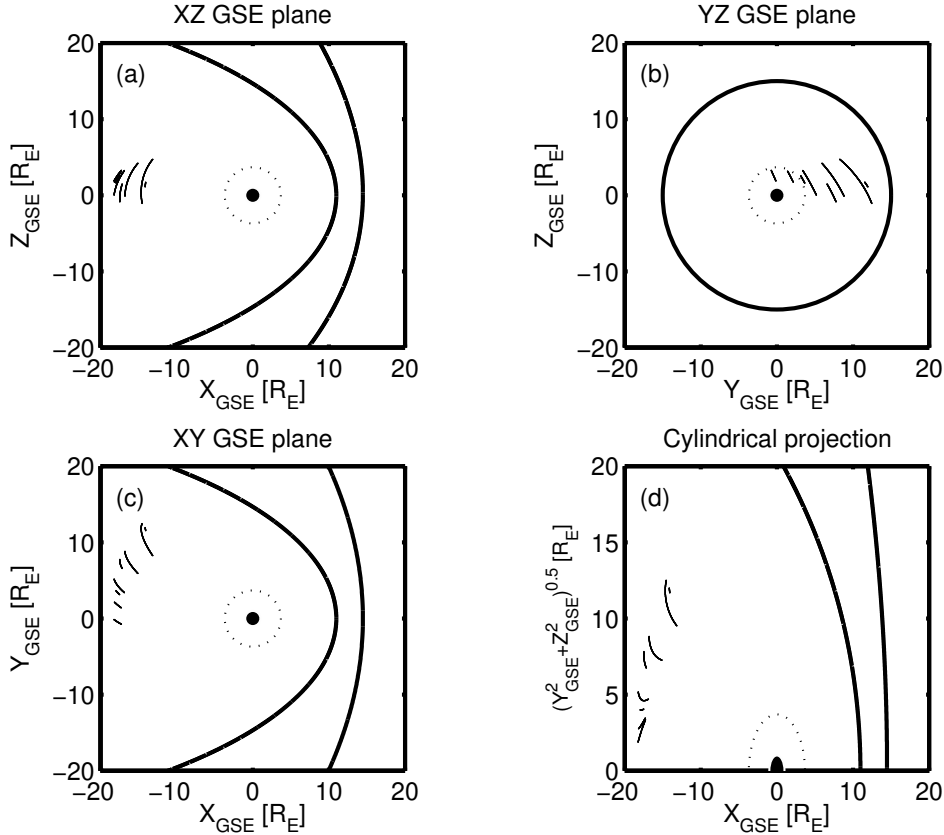
904 **Figure 9.** Scattered plots of the Cluster SC3 and GUMICS-4 simulations for all intervals in
 905 the magnetosheath in GSE system. The dashed line is the $y=x$ line. (a) Magnetic field Z com-
 906 ponent. (b) Solar wind velocity X component. (c) Solar wind density measured by the CIS HIA
 907 instrument (red) and calculated from the spacecraft potential (blue).



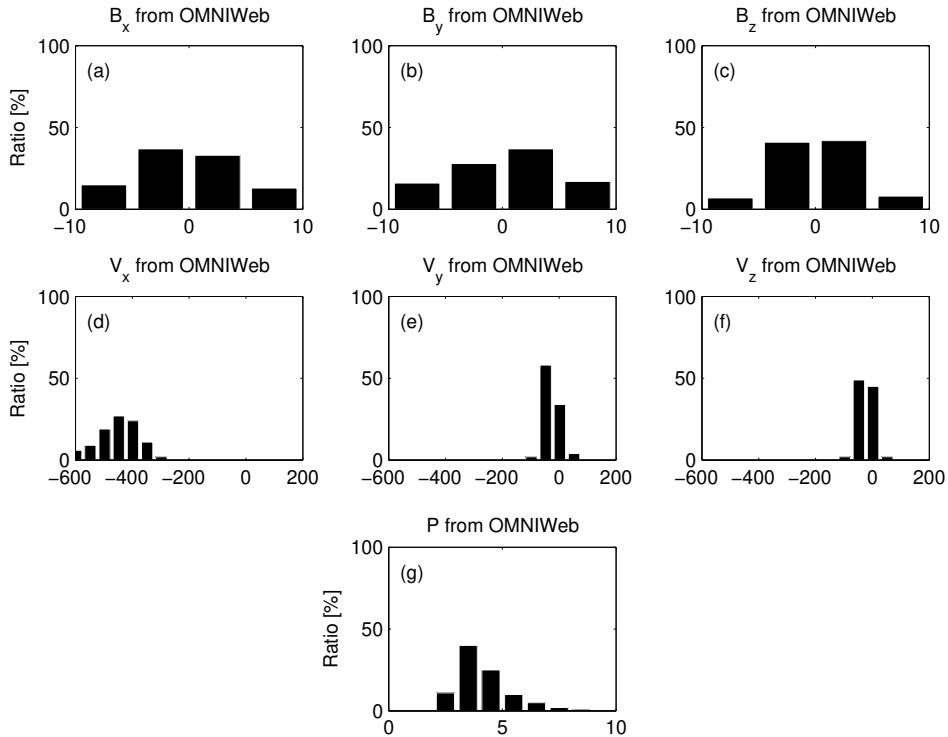
908 **Figure 10.** The distributions of the correlation coefficients (a, c, e, g) of the magnetic field Z
 909 component (B_z) in GSE system, solar wind velocity X component (V_X) in GSE system, the solar
 910 wind density measured by the CIS HIA (n_{CIS}) instrument and calculated from the spacecraft
 911 potential (n_{EFW}), respectively, for all intervals in the magnetosheath. The distributions of the
 912 time shifts (b, d, f, h) of the B_z , the V_X , the n_{CIS} and the n_{EFW}), respectively, for all intervals
 913 in the magnetosheath.



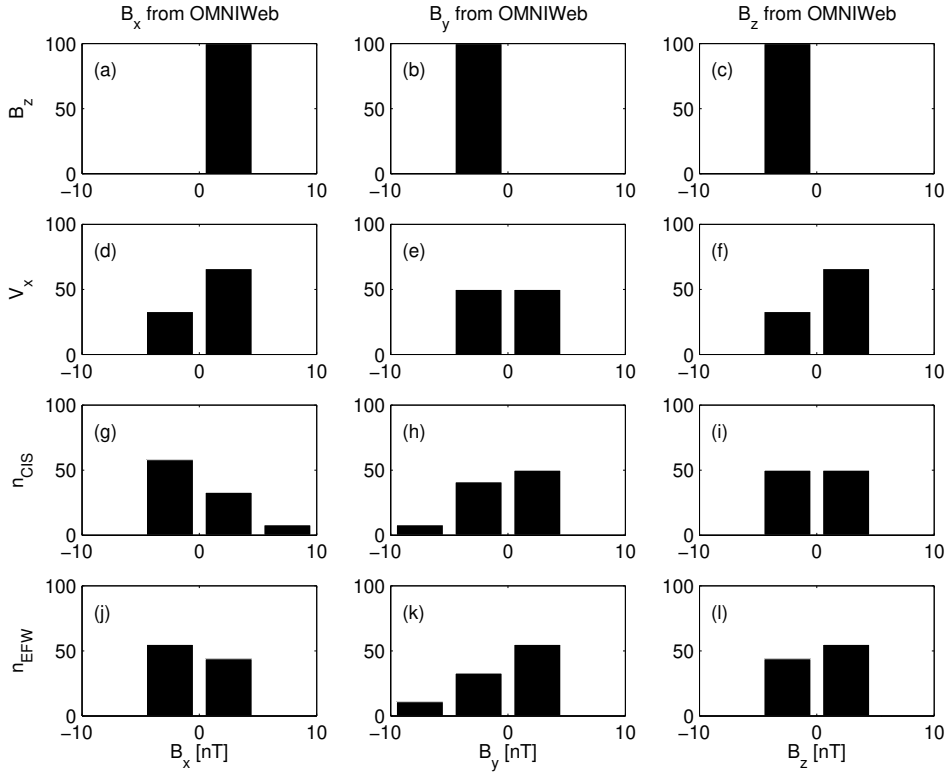
914 **Figure 11.** Cluster SC3 orbit in the magnetosphere in GSE system for all intervals (see Ta-
 915 ble 3). (a) XZ (b) YZ (c) XY (d) Cylindrical projection. Average bow-shock and magnetopause
 916 positions are drawn on all plots using solid line [Peredo *et al.*, 1995; Tsyganenko, 1995, respec-
 917 tively]. The black dots at $3.7 R_E$ show the boundary of the GUMICS-4 inner magnetospheric
 918 domain. The black circle in the origo of all plots shows the size of the Earth.



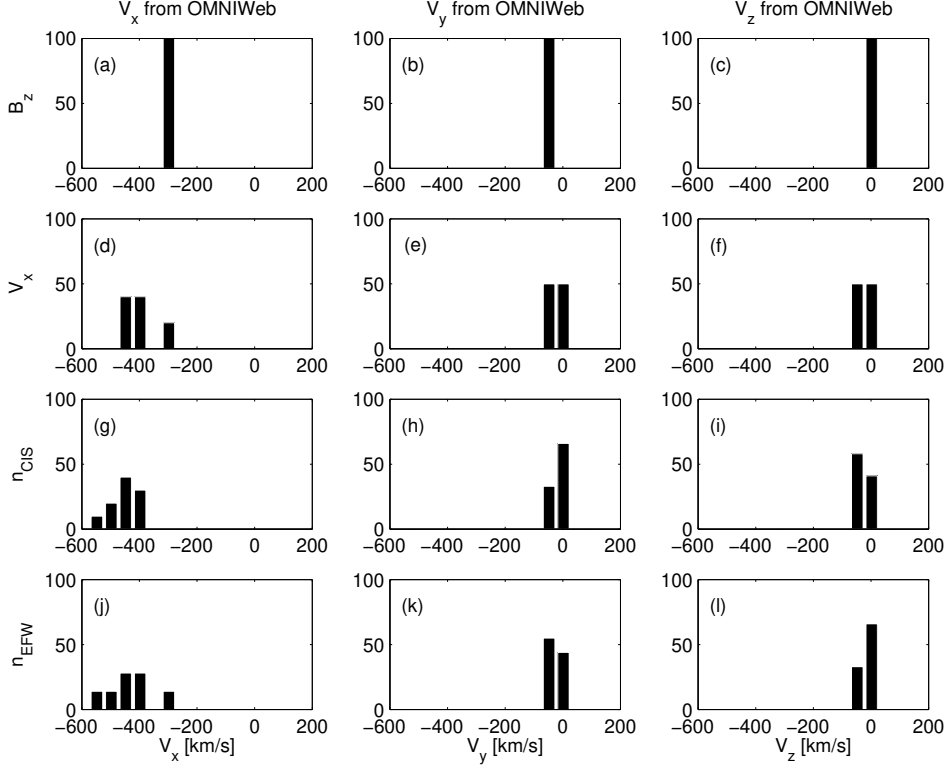
919 **Figure 12.** Cluster SC3 orbit in the tail in GSE system for all intervals (see Table 6). (a)
 920 (b) (c) (d) Cylindrical projection. Average bow-shock and magnetopause positions
 921 are drawn on all plots using solid line [Perego *et al.*, 1995; Tsyganenko, 1995, respectively]. The
 922 black dots at $3.7 R_E$ show the boundary of the GUMICS–4 inner magnetospheric domain. The
 923 black circle in the origo of all plots shows the size of the Earth.



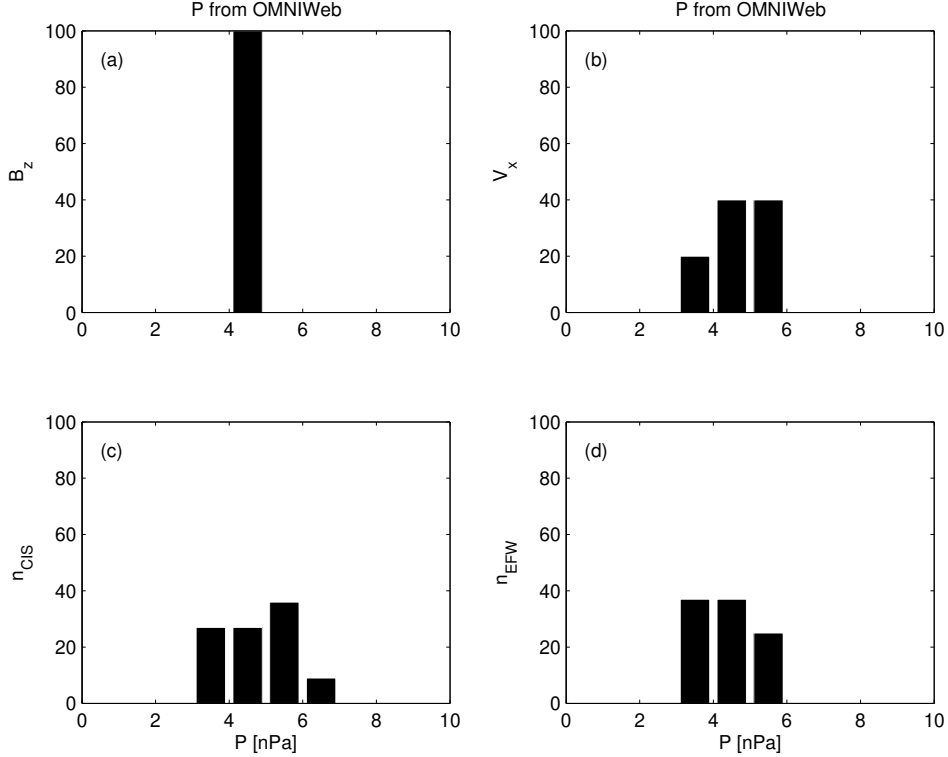
924 **Figure 13.** (a, b, c) The distributions of the OMNI solar wind magnetic field (B_x , B_y , B_z)
 925 components, (d, e, f) the OMNI solar wind velocity (V_x , V_y , V_z) components and (g) the solar
 926 wind dynamic pressure during the 1-year run from January 29, 2002 to February 2, 2003 in GSE
 927 reference frame, respectively. The relative values are given on the vertical axis of all plots in
 928 percentage.



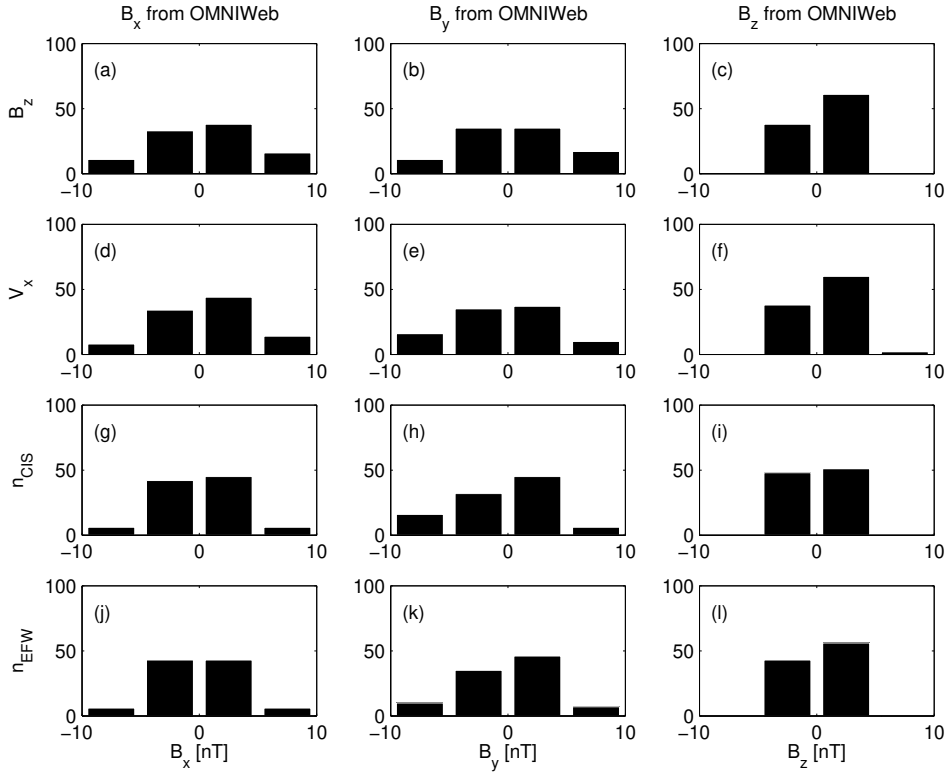
929 **Figure 14.** The distributions of the B_x , the B_y and the B_z OMNI solar wind magnetic field
 930 components when the agreement of the Cluster SC3 measurements and the GUMICS–4 simu-
 931 lations are poor in the solar wind (see Table 4). The B_z , the V_x , the n_{CIS} and the n_{EFW} are
 932 the magnetic field GSE Z component, the plasma ion velocity X GSE component, the solar wind
 933 density measured by the CIS HIA instrument and the calculated from the EFW spacecraft po-
 934 tential, respectively. (a, b, c) Distribution of OMNI B_x , B_y , B_z when the agreement of B_z is
 935 poor. (d, e, f) Distribution of OMNI B_x , B_y , B_z when the agreement of V_x is poor. (g, h, i)
 936 Distribution of OMNI B_x , B_y , B_z when the agreement of n_{CIS} is poor. (j, k, l) Distribution of
 937 OMNI B_x , B_y , B_z when the agreement of n_{EFW} is poor. The values are in percentage unit in
 938 the distributions.



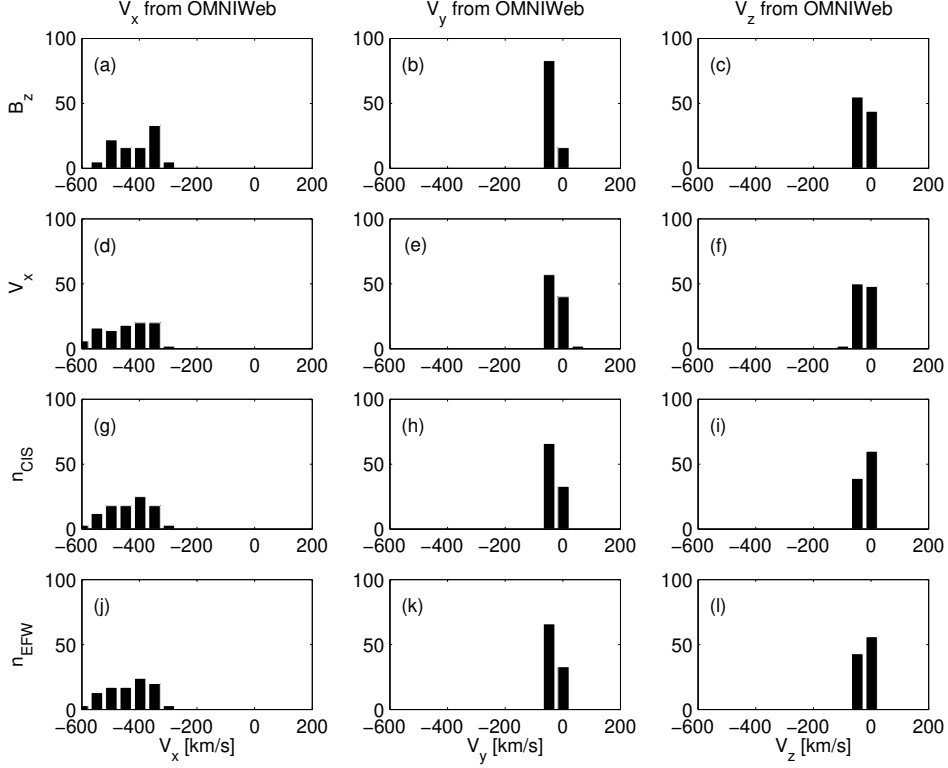
939 **Figure 15.** The distributions of the V_x , the V_y and the V_z OMNI solar wind magnetic field
940 components when the agreement of the Cluster SC3 measurements and the GUMICS–4 simu-
941 lations are poor in the solar wind (see Table 4). The B_z , the V_x , the n_{CIS} and the n_{EFW} are
942 the magnetic field GSE Z component, the plasma ion velocity X GSE component, the solar wind
943 density measured by the CIS HIA instrument and the calculated from the EFW spacecraft po-
944 tential, respectively. (a, b, c) Distribution of OMNI V_x , V_y , V_z when the agreement of B_z is poor.
945 (d, e, f) Distribution of OMNI V_x , V_y , V_z when the agreement of V_x is poor. (g, h, i) Distribution
946 of OMNI V_x , V_y , V_z when the agreement of n_{CIS} is poor. (j, k, l) Distribution of OMNI V_x , V_y ,
947 V_z when the agreement of n_{EFW} is poor. The values are in percentage unit in the distributions.



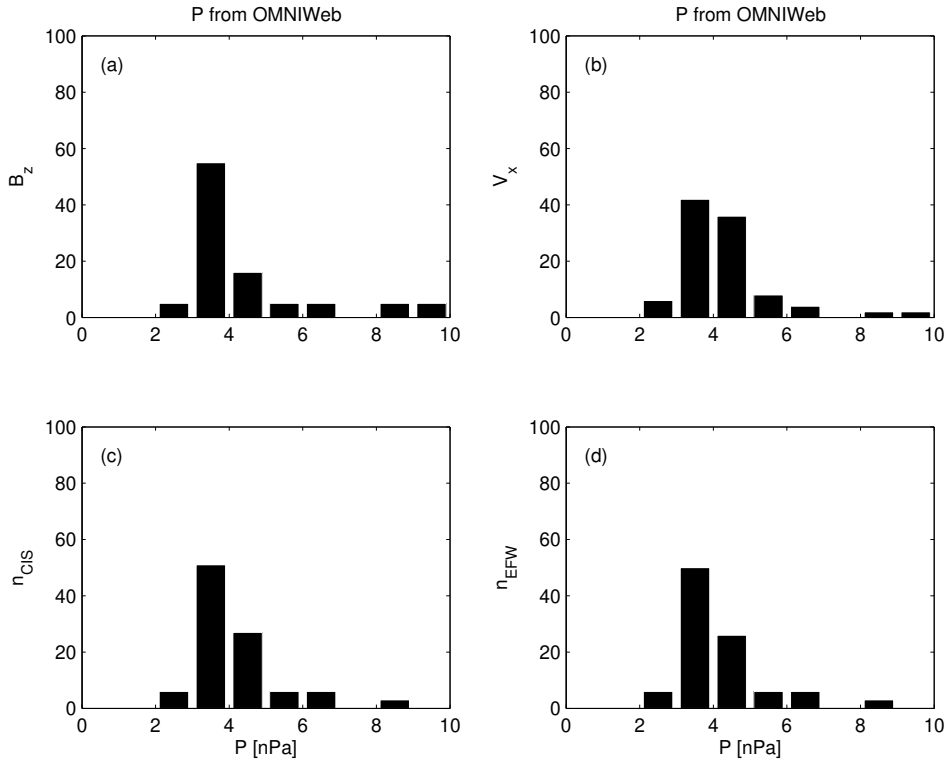
948 **Figure 16.** The distributions of the P solar wind dynamic pressure calculated from OMNI
 949 parameters when the agreement of the Cluster SC3 measurements and the GUMICS–4 simula-
 950 tions are poor in the solar wind (see Table 4). The B_z , V_x , n_{CIS} and n_{EFW} are the magnetic
 951 field GSE Z component, the velocity X GSE component, the solar wind density measured by the
 952 CIS HIA instrument and calculated from the EFW spacecraft potential, respectively. (a, b, c, d)
 953 The distribution of the P calculated from OMNI data when the agreement of the B_z , the V_x , the
 954 n_{CIS} or the n_{EFW} are poor. The values are in percentage unit in the distributions.



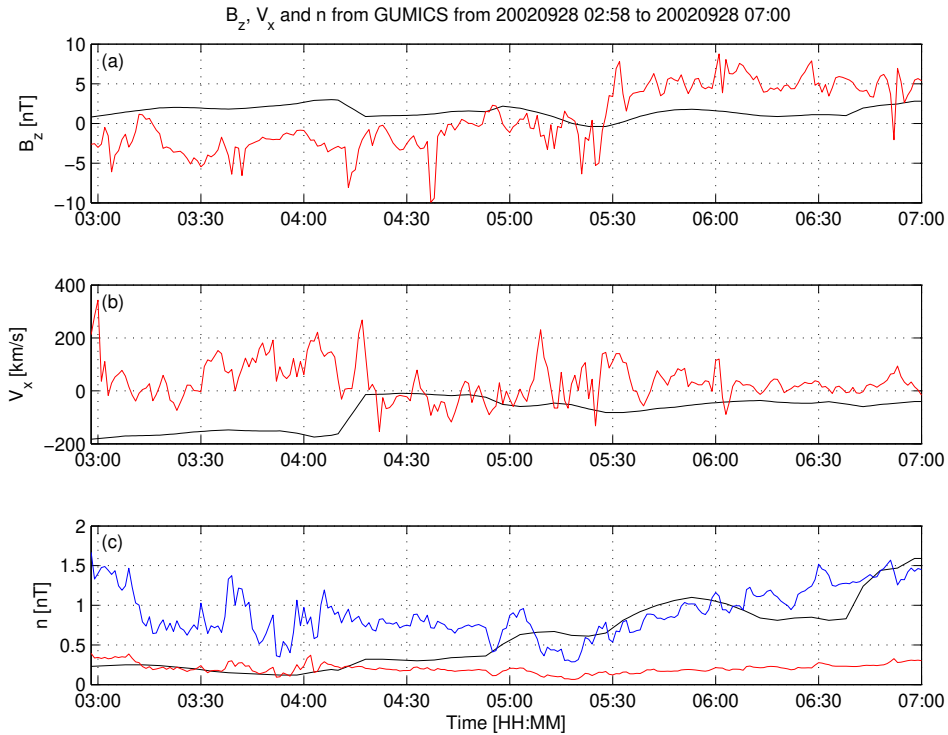
955 **Figure 17.** The distributions of the B_x , the B_y and the B_z OMNI solar wind magnetic field
956 components when the agreement of the Cluster SC3 measurements and the GUMICS–4 simu-
957 lations are poor in the magnetosheath (see Table 5). The B_z , the V_x , the n_{CIS} and the n_{EFW}
958 are the magnetic field GSE Z component, the plasma ion velocity X GSE component, the solar
959 wind density measured by the CIS HIA instrument and the calculated from the EFW spacecraf-
960 t potential, respectively. (a, b, c) Distribution of OMNI B_x , B_y , B_z when the agreement of B_z
961 is poor. (d, e, f) Distribution of OMNI B_x , B_y , B_z when the agreement of V_x is poor. (g, h, i)
962 Distribution of OMNI B_x , B_y , B_z when the agreement of n_{CIS} is poor. (j, k, l) Distribution of
963 OMNI B_x , B_y , B_z when the agreement of n_{EFW} is poor. The values are in percentage unit in
964 the distributions.



965 **Figure 18.** The distributions of the V_x , the V_y and the V_z OMNI solar wind magnetic field
966 components when the agreement of the Cluster SC3 measurements and the GUMICS–4 simula-
967 tions are poor in the magnetosheath (see Table 5). The B_z , the V_x , the n_{CIS} and the n_{EFW} are
968 the magnetic field GSE Z component, the plasma ion velocity X GSE component, the solar wind
969 density measured by the CIS HIA instrument and the calculated from the EFW spacecraft po-
970 tential, respectively. (a, b, c) Distribution of OMNI V_x , V_y , V_z when the agreement of B_z is poor.
971 (d, e, f) Distribution of OMNI V_x , V_y , V_z when the agreement of V_x is poor. (g, h, i) Distribution
972 of OMNI V_x , V_y , V_z when the agreement of n_{CIS} is poor. (j, k, l) Distribution of OMNI V_x , V_y ,
973 V_z when the agreement of n_{EFW} is poor. The values are in percentage unit in the distributions.



974 **Figure 19.** The distributions of the P solar wind dynamic pressure calculated from OMNI pa-
 975 rameters when the agreement of the Cluster SC3 measurements and the GUMICS-4 simulations
 976 are poor in the magnetosheath (see Table 5). The B_z , V_x , n_{CIS} and n_{EFW} are the magnetic
 977 field GSE Z component, the velocity X GSE component, the solar wind density measured by the
 978 CIS HIA instrument and calculated from the EFW spacecraft potential, respectively. (a, b, c, d)
 979 The distribution of the P calculated from OMNI data when the agreement of the B_z , the V_x , the
 980 n_{CIS} or the n_{EFW} are poor. The values are in percentage unit in the distributions.



981 **Figure 20.** GUMICS-4 simulation results (black) and Cluster SC3 magnetic field Z compo-
 982 nent, ion plasma moments (red) and electron density calculated from spacecraft potential (blue)
 983 from September 28, 2002 from 2:58 to 7:00 (UT) in the tail in GSE system. (a) Magnetic field
 984 Z component. (b) Solar wind velocity X component (c) Solar wind density. From 05:15 to 05:30
 985 both the Cluster SC3 and the virtual spaceprobe of the GUMICS-4 simulation cross the neutral
 986 sheet multiple times.

Start/End	C_{B_z}	δt_{B_z}	C_{V_x}	δt_{V_x}	$C_{n_{CIS}}$	$\delta t_{n_{CIS}}$	$C_{n_{EFW}}$	$\delta t_{n_{EFW}}$
	[min]		[min]		[min]		[min]	
20020201 20:00/0203 04:00	0.96	2	1.00	13	0.96	3	0.98	3
20020211 13:00/0212 12:00	0.82	2	1.00	0	0.99	18	0.99	18
20020218 09:00/0219 02:00	0.93	0	1.00	-3	0.94	-3	0.97	-3
20020219 06:30/0219 15:00	0.93	1	1.00	0	0.99	-60	1.00	-52
20020220 18:30/0222 00:00	0.87	4	1.00	4	0.93	-21	0.98	3
20020318 17:30/0319 02:30	0.89	1	1.00	21	0.98	50	0.99	5
20020412 20:30/0413 02:00	0.90	4	0.99	-54	0.94	60	0.98	12
20021227 12:00/1228 03:00	0.75	4	1.00	-3	0.99	-26	0.99	21
20021229 20:00/1230 16:00	0.68	1	1.00	1	0.99	-30	0.98	41
20030106 06:00/0106 19:00	0.79	4	1.00	6	0.99	4	0.99	-60
20030108 07:00/0109 03:30	0.55	10	1.00	41	0.99	10	0.97	-55
20030113 08:30/0113 18:00	0.91	3	1.00	5	1.00	3	0.97	-1
20030120 07:30/0120 13:00	0.82	2	1.00	9	1.00	-6	1.00	-3
20030122 12:00/0123 14:00	0.81	2	1.00	3	0.99	3	0.92	-60
20030124 18:00/0126 00:00	0.73	3	1.00	0	0.99	-60	0.99	60
20030127 16:00/0128 06:00	0.88	-1	1.00	-3	0.95	1	0.88	11
20030129 12:00/0130 18:00	0.90	2	1.00	4	0.94	-59	0.98	1

987 **Table 1.** The studied solar wind intervals. The correlation coefficients (C_{B_z} , C_{V_x} , $C_{n_{CIS}}$,
988 $C_{n_{EFW}}$) and time shift (δt_{V_x} , $\delta t_{n_{CIS}}$, $\delta t_{n_{EFW}}$) in minutes of the magnetic field GSE Z compo-
989 nent (B_z), solar wind velocity X component (V_x), CIS and EFW densities (n_{CIS} , n_{EFW}).

Table 2: The studied magnetosheath intervals. The correlation coefficients (C_{B_z} , C_{V_x} , $C_{n_{CIS}}$, $C_{n_{EFW}}$) and time shift (δt_{V_x} , $\delta t_{n_{CIS}}$, $\delta t_{n_{EFW}}$) in minutes of the magnetic field GSE Z component (B_z), solar wind velocity X component (V_x), CIS and EFW densities (n_{CIS} , n_{EFW}). In the empty slots the correlation calculation gives invalid result.

Start/End	C_{B_z}	δt_{B_z}	C_{V_x}	δt_{V_x}	$C_{n_{CIS}}$	$\delta t_{n_{CIS}}$	$C_{n_{EFW}}$	$\delta t_{n_{EFW}}$
		[min]		[min]		[min]		[min]
20020201 13:30/0201 18:30	0.91	1	0.98	56	0.99	60	0.976	60
20020208 18:15/0209 00:00	0.73	2	0.95	60	0.98	-52	0.98	-54
20020211 02:30/0211 09:00	0.79	0	0.99	-20	0.99	-1	0.99	1
20020212 16:30/0212 21:00	0.80	3	0.99	54	0.99	31	0.99	30
20020219 17:30/0219 23:00	0.76	4	0.98	37	0.99	7	0.99	6
20020222 23:00/0223 06:30	0.64	0	0.97	-60	0.99	-47	0.98	-48
20020227 16:30/0227 23:15	0.48	59	0.98	-31	0.99	-39	1.00	-12
20020310 18:30/0311 00:30	0.97	3	0.98	19	0.99	8	0.99	-2
20020311 14:00/0311 19:00	0.86	5	0.97	36	0.99	-3	0.99	-40
20020406 19:00/0407 01:15	0.76	2	0.96	-60	0.98	-55	0.98	-56
20020410 17:30/0410 23:00	0.89	6	0.99	-50	0.99	3	1.00	5
20020411 11:30/0411 16:30	0.82	4	0.99	39	0.99	3	0.99	3
20020418 18:30/0418 22:45	0.92	60	0.99	-60	0.99	60	0.98	60
20020421 04:30/0421 07:45	0.96	47	0.99	-60	1.00	-60	1.00	-60
20020422 11:45/0422 15:45	0.73	-5	0.98	-17	0.99	-15	0.98	-16
20020423 08:30/0423 12:30	0.93	31	0.99	3	0.99	16	0.99	16
20020430 12:30/0430 17:00	0.79	59	0.98	22	0.98	-18		
20020505 07:00/0505 11:15	0.71	59	0.99	-58	0.98	-60		
20020506 19:15/0507 00:15	0.84	-27	0.98	-60	0.97	-37		
20020507 17:30/0507 23:00	0.93	2	0.98	-30	0.99	-49		
20020514 22:45/0515 03:00	0.79	49	0.99	35	0.99	38	0.99	43
20020517 07:00/0517 12:15	0.74	-5	1.00	-5	0.99	-4	0.99	-3
20020518 13:30/0518 19:30	0.70	1	0.99	9	0.97	-1	0.97	-1

Continued on next page

Table 2 – *Continued from previous page*

Start/End	C_{B_z}	δt_{B_z}	C_{V_x}	δt_{V_x}	$C_{n_{CIS}}$	$\delta t_{n_{CIS}}$	$C_{n_{EFW}}$	$\delta t_{n_{EFW}}$
		[min]		[min]		[min]		[min]
20020519 20:00/0520 03:30	0.98	2	1.00	-9	0.99	-5	0.99	-50
20020520 10:45/0520 20:15	0.77	1	0.99	-3	0.95	-1	0.99	-1
20020522 02:00/0522 08:45	0.49	52	0.99	4	0.99	12	0.99	22
20020527 02:15/0527 17:15	0.79	-3	0.99	-3	0.98	0	0.98	0
20020530 05:00/0530 10:30	0.29	3	1.00	-38	0.99	3	0.99	3
20020601 19:30/0602 01:00	0.68	-2	1.00	18	0.99	-6	0.99	-7
20020602 21:45/0603 17:45	0.62	-5	0.99	-1	0.98	2	0.99	2
20020605 10:30/0606 06:00	0.18	0	1.00	-7	0.97	10	0.98	9
20020607 18:00/0607 22:00	0.92	-35	1.00	-36	0.99	16	0.99	16
20020608 01:15/0608 18:15	0.53	-4	0.99	-39	0.96	-6	0.97	-6
20020610 01:30/0610 09:30	0.76	5	0.99	8	0.99	-5	0.99	-7
20020610 11:00/0611 01:00	0.87	-4	0.99	-33	0.98	23	0.99	6
20020612 18:30/0613 06:15	0.44	-2	0.99	-7	0.97	4	0.97	-32
20020615 07:00/0615 23:30			1.00	47	0.98	-3	0.98	-3
20020617 05:00/0618 03:45	0.76	4	1.00	28	0.98	10	0.98	8
20020620 04:00/0620 11:00	0.61	-8	0.99	-6	0.97	12	0.98	4
20020622 14:30/0622 18:00	0.98	55	1.00	35	0.99	16	1.00	16
20021201 04:15/1202 07:45	0.38	1	1.00	2	0.99	6	0.99	6
20021203 15:30/1204 19:30	0.67	1	0.99	60	0.98	59	0.98	59
20021207 00:30/1207 07:45	0.49	37	0.98	-56	0.99	-19	0.99	-4
20021208 09:30/1209 08:00	0.69	2	0.98	-35	0.97	6	0.98	4
20021212 23:30/1213 14:30	0.51	5	1.00	36	0.99	-3	0.81	-56
20021213 21:15/1214 09:30	0.93	5	0.99	-35	0.99	-13	0.99	-47
20021215 12:45/1216 18:00	0.76	2	0.99	-60	0.94	-60	0.98	31
20021217 16:30/1218 01:45	0.99	2	1.00	-54	0.99	3	0.99	3
20021220 01:30/1220 06:15	0.92	0	1.00	60	0.99	2	0.99	3
20021223 02:15/1223 13:00	0.91	1	0.97	49	0.93	49	0.99	-14
20021223 14:00/1223 22:30	0.84	1	0.99	-2	0.99	-1	1.00	-3
20021224 19:00/1225 01:45	0.94	0	1.00	-44	0.99	26	0.99	27

Continued on next page

Table 2 – *Continued from previous page*

Start/End	C_{B_z}	δt_{B_z}	C_{V_x}	δt_{V_x}	$C_{n_{CIS}}$	$\delta t_{n_{CIS}}$	$C_{n_{EFW}}$	$\delta t_{n_{EFW}}$
		[min]		[min]		[min]		[min]
20021225 23:45/1226 07:15	0.96	7	1.00	-17	0.99	56	0.99	55
20021226 23:00/1227 09:45	0.79	2	1.00	2	0.98	4	0.99	3
20021229 11:45/1229 17:00	0.60	2	1.00	-60	0.98	-19	0.98	50
20021230 17:45/1231 01:00	0.69	1	0.98	52	0.98	60	0.98	22
20021231 23:00/0101 05:15	0.89	2	0.99	15	0.99	-54	1.00	-58
20030105 14:00/0105 21:00	0.69	0	0.99	1	0.98	-60	0.99	-60
20030106 23:15/0107 03:00	0.52	9	0.98	60	0.99	56	1.00	-60
20030109 08:45/0109 16:15			0.91	-56	0.98	-13	0.98	-26
20030110 07:15/0110 15:15	0.94	1	0.99	-7	0.99	1	0.98	5
20030111 08:15/0111 22:30	0.84	0	0.99	-59	0.94	-15	0.94	8
20030112 17:30/0113 00:15	0.98	0	1.00	-52	0.99	39	0.99	51
20030114 00:30/0114 08:30	0.84	-1	0.99	-60	0.98	23	0.98	8
20030116 10:15/0116 17:45	0.62	60	0.93	52	0.99	60	0.99	30
20030117 09:30/0117 13:30	0.68	-3	1.00	8	1.00	-31	0.99	-33
20030118 23:30/0119 03:45	0.93	3	1.00	-12	1.00	7	0.99	7
20030119 21:00/0120 01:00	0.94	3	1.00	5	1.00	38	1.00	19
20030121 06:30/0121 11:30	0.82	-15	0.96	47	0.98	7	0.99	-39
20030122 04:45/0122 09:30	0.69	-2	1.00	10	0.99	-9	0.99	-5
20030126 01:45/0126 06:30	0.85	3	0.99	-15	0.99	-50	0.99	23
20030127 08:15/0127 13:00	1.00	9	1.00	-60	0.98	0	0.99	1
20030128 12:30/0128 17:15	0.77	60	0.99	-24	0.99	-6	0.988	20
20030130 19:45/0131 00:15	0.98	2	0.99	51	0.99	25	0.99	9

Table 3: The studied magnetosphere intervals (UT).

Start/End
20020213 23:00/0214 01:30
20020217 18:30/0218 02:00
20020220 00:45/0220 12:00
20020222 11:15/0222 20:15
20020225 02:15/0225 08:30
20020227 06:00/0227 12:00
20020302 00:00/0302 03:15
20020306 10:00/0306 18:30
20020308 17:30/0309 06:00
20020311 02:15/0311 12:00
20020313 11:15/0314 00:15
20020316 04:45/0316 08:00
20020318 09:00/0318 14:45
20020320 20:30/0320 23:55
20020323 04:00/0323 09:45
20020327 23:45/0328 06:15
20020330 07:15/0330 12:45
20020401 19:30/0401 22:00
20020406 09:30/0406 18:00
20020408 15:00/0409 00:00
20020410 23:30/0411 09:45
20020413 08:30/0413 19:00
20020416 18:00/0417 04:30
20020418 06:00/0418 12:00
20020420 15:00/0420 23:00
20020422 20:00/0423 07:00
20020425 08:30/0425 18:00
20020430 04:40/0430 12:00
20020504 14:30/0504 16:45

Continued on next page

Table 3 – *Continued from previous page*

Start/End
20020505 02:30/0505 07:00
20020507 01:30/0507 15:45
20020508 11:00/0510 04:15
20020512 02:45/0512 09:30
20020514 10:30/0514 12:45
20020519 00:30/0519 19:30
20020521 01:30/0521 22:00
20020523 23:30/0524 02:00
20020524 19:00/0525 08:15
20020526 07:30/0526 10:30
20020528 20:00/0529 05:00
20020531 02:15/0531 13:30
20020602 04:30/0602 07:30
20020602 12:00/0602 21:30
20020604 08:30/0605 07:00
20020606 14:30/0607 16:30
20020609 06:00/0609 20:00
20020611 11:00/0612 13:00
20020614 01:00/0614 16:00
20020616 08:00/0616 18:00
20020620 13:30/0622 01:00
20020623 13:00/0623 17:00
20020624 04:00/0624 10:15
20020630 17:45/0701 15:00
20020701 21:00/0703 10:30
20020703 23:00/0706 03:15
20020707 01:00/0708 23:00
20020710 11:30/0714 03:30
20020714 15:45/0715 15:30
20020716 23:30/0717 16:00

Continued on next page

Table 3 – *Continued from previous page*

Start/End
20020718 05:45/0722 11:00
20020722 23:45/0728 01:00
20020728 02:00/0804 03:45
20020804 04:45/0811 06:15
20020811 07:30/0816 01:00
20020816 15:30/0818 09:00
20020818 10:00/0825 11:30
20020825 13:00/0901 14:15
20020901 17:15/0903 23:30
20020905 02:15/0906 16:30
20020907 10:30/0908 17:00
20020908 18:00/0915 19:30
20020915 21:00/0922 22:30
20020923 00:00/0923 23:30
20020924 03:30/0928 22:45
20020928 23:30/0930 01:00
20020930 02:15/1006 17:00
20021006 17:45/1007 03:30
20021007 05:00/1007 17:30
20021008 07:30/1010 22:00
20021010 22:30/1012 22:30
20021012 23:00/1014 06:30
20021014 09:00/1016 04:00
20021016 14:00/1019 00:15
20021019 01:30/1019 22:00
20021021 04:00/1022 19:30
20021022 22:30/1026 02:30
20021026 04:00/1029 20:15
20021030 01:30/1102 08:00
20021102 22:00/1104 22:00

Continued on next page

Table 3 – *Continued from previous page*

Start/End
20021106 00:00/1107 18:00
20021108 02:00/1109 18:45
20021111 00:00/1112 01:30
20021113 03:45/1114 14:15
20021115 20:30/1116 23:00
20021118 01:00/1118 23:30
20021120 17:00/1121 06:00
20021122 21:30/1124 01:00
20021125 04:00/1126 08:30
20021127 20:00/1128 18:30
20021130 04:00/1201 01:30
20021202 14:30/1203 09:00
20021204 22:00/1205 19:30
20021207 09:00/1207 16:30
20021207 18:00/1207 22:00
20021209 16:30/1210 14:30
20021212 13:45/1212 21:30
20021214 13:30/1214 20:00
20021214 21:00/1215 07:30
20021216 21:00/1217 15:00
20021219 08:00/1219 19:30
20021221 15:45/1221 23:15
20021222 00:30/1222 08:45
20021224 02:30/1224 14:00
20021226 10:00/1226 19:00
20021228 19:30/1229 02:30
20021229 04:00/1229 10:00
20021231 05:00/1231 18:45
20030102 12:30/0102 20:45
20030104 20:45/0105 06:00

Continued on next page

Table 3 – *Continued from previous page*

Start/End
20030105 07:00/0105 13:30
20030107 05:45/0107 21:00
20030109 17:00/0110 00:45
20030112 00:00/0112 09:15
20030112 10:30/0112 16:00
20030114 11:00/0114 20:00
20030116 20:30/0116 22:45
20030119 04:30/0119 09:30
20030119 14:00/0119 17:00
20030121 13:30/0121 21:30
20030126 07:30/0126 15:45
20030128 17:45/0129 08:15
20030131 01:30/0131 11:45

Start/End	OMNI			Cluster SC3			
	B_z [nT]	V_x [km/s]	P [cm $^{-3}$]	B_z	V_x	n_{CIS}	n_{EFW}
20020201 20:00/0203 04:00	-1.25	-373.52	4.08	y	y	n	y
20020211 13:00/0212 12:00	0.03	-533.11	2.18	y	y	y	y
20020218 09:00/0219 02:00	2.56	-362.41	3.46	y	n	n	y
20020219 06:30/0219 15:00	3.55	-401.63	1.25	y	y	n	n
20020220 18:30/0222 00:00	1.95	-440.18	1.96	y	y	n	y
20020318 17:30/0319 02:30	3.79	-429.30	15.34	y	n	n	n
20020412 20:30/0413 02:00	-1.81	-420.35	3.24	y	n	n	y
20021227 12:00/1228 03:00	0.09	-714.40	2.72	y	n	n	y
20021229 20:00/1230 16:00	-0.37	-526.40	2.26	y	y	n	n
20030106 06:00/0106 19:00	2.25	-399.91	1.50	y	n	n	n
20030108 07:00/0109 03:30	-0.58	-280.80	2.97	n	n	y	n
20030113 08:30/0113 18:00	0.68	-397.83	1.72	y	y	y	n
20030120 07:30/0120 13:00	2.16	-630.69	2.43	y	y	y	y
20030122 12:00/0123 14:00	0.13	-608.96	3.41	y	y	y	n
20030124 18:00/0126 00:00	-0.71	-739.68	2.87	y	y	n	n
20030127 16:00/0128 06:00	-0.92	-451.84	3.12	y	y	n	n
20030129 12:00/0130 18:00	-3.09	-450.00	3.96	y	y	n	y

992 **Table 4.** The average OMNI input parameters in the solar wind and the good/bad agreement
993 of the GUMICS–4 simulations to the Cluster B_z magnetic field component, the V_x solar wind
994 speed component, the n_{CIS} solar wind density measured by the Cluster CIS HIA instrument and
995 the n_{EFW} solar wind density calculated from the spacecraft potential measured by the Cluster
996 EFW instrument in the solar wind.

Table 5: The average OMNI input parameters in the solar wind and the good/bad agreement of the GUMICS–4 simulations to the Cluster B_z magnetic field component, the V_x solar wind speed component, the n_{CIS} solar wind density measured by the Cluster CIS HIA instrument and the n_{EFW} solar wind density calculated from the spacecraft potential measured by the Cluster EFW instrument in the magnetosheath.

Start/End	OMNI			Cluster SC3			
	B_z	V_x	P	B_z	V_x	n_{CIS}	n_{EFW}
	[nT]	[km/s]	[cm $^{-3}$]				
20020201 13:30/0201 18:30	0.19	-342.87	4.62	y	n	n	n
20020208 18:15/0209 00:00	-0.48	-508.16	1.61	y	n	n	n
20020211 02:30/0211 09:00	-1.85	-425.67	1.78	y	y	y	y
20020212 16:30/0212 21:00	2.98	-509.22	2.34	y	n	n	n
20020219 17:30/0219 23:00	1.46	-431.50	1.46	y	y	y	y
20020222 23:00/0223 06:30	0.86	-391.22	1.14	y	n	n	n
20020227 16:30/0227 23:15	1.89	-343.13	1.52	n	n	n	n
20020310 18:30/0311 00:30	-2.81	-379.46	1.78	y	y	y	y
20020311 14:00/0311 19:00	1.63	-371.43	2.68	n	n	n	n
20020406 19:00/0407 01:15	-2.71	-333.13	0.93	y	n	n	n
20020410 17:30/0410 23:00	0.31	-312.43	4.42	n	n	y	y
20020411 11:30/0411 16:30	-1.50	-494.02	4.25	y	y	n	n
20020418 18:30/0418 22:45	-0.92	-450.82	0.30	n	n	n	n
20020421 04:30/0421 07:45	0.40	-455.69	1.37	n	n	n	n
20020422 11:45/0422 15:45	0.25	-419.98	1.14	n	n	y	y
20020423 08:30/0423 12:30	2.77	-507.99	6.82	n	n	n	n
20020430 12:30/0430 17:00	2.15	-479.51	3.02	n	n	n	n
20020505 07:00/0505 11:15	0.20	-336.81	1.74	n	n	n	n
20020506 19:15/0507 00:15	0.78	-390.00	2.46	y	n	n	n
20020507 17:30/0507 23:00	2.87	-392.40	3.49	y	n	n	n
20020514 22:45/0515 03:00	-2.42	-414.01	1.82	n	n	n	n

Continued on next page

Table 5 – *Continued from previous page*

Start/End	OMNI			Cluster SC3			
	B_z [nT]	V_x [km/s]	P $[cm^{-3}]$	B_z	V_x	n_{CIS}	n_{EFW}
20020517 07:00/0517 12:15	-0.39	-379.32	1.52	y	y	y	y
20020518 13:30/0518 19:30	0.63	-345.87	1.59	n	n	y	y
20020519 20:00/0520 03:30	4.75	-408.56	1.12	y	y	y	y
20020520 10:45/0520 20:15	0.74	-448.89	1.93	y	y	y	y
20020522 02:00/0522 08:45	-1.07	-398.12	1.63	n	y	y	y
20020527 02:15/0527 17:15	-3.11	-542.53	2.07	y	y	y	y
20020530 05:00/0530 10:30	0.03	-493.86	2.08	y	n	y	y
20020601 19:30/0602 01:00	-3.38	-342.27	4.16	y	y	y	y
20020602 21:45/0603 17:45	0.38	-435.47	1.89	y	y	y	y
20020605 10:30/0606 06:00	-0.42	-394.49	1.08	y	y	n	n
20020607 18:00/0607 22:00	-1.60	-291.85	1.80	y	y	y	y
20020608 01:15/0608 18:15	0.06	-335.39	2.74	y	n	y	y
20020610 01:30/0610 09:30	1.60	-465.52	3.00	y	y	y	y
20020610 11:00/0611 01:00	-2.27	-419.86	2.16	y	n	y	y
20020612 18:30/0613 06:15	-1.13	-351.03	1.16	y	y	y	y
20020615 07:00/0615 23:30	-1.16	-334.27	2.84	n	n	y	y
20020617 05:00/0618 03:45	0.78	-351.47	1.87	y	n	y	y
20020620 04:00/0620 11:00	0.46	-485.48	1.73	y	y	y	y
20020622 14:30/0622 18:00	-0.72	-429.02	1.93	n	n	y	y
20021201 04:15/1202 07:45	-1.09	-499.23	2.62	y	y	y	y
20021203 15:30/1204 19:30	0.34	-449.09	2.06	y	n	n	n
20021207 00:30/1207 07:45	0.80	-451.80	7.33	n	n	y	y
20021208 09:30/1209 08:00	0.60	-600.27	1.49	y	n	y	y
20021212 23:30/1213 14:30	0.10	-337.77	1.32	y	n	n	n
20021213 21:15/1214 09:30	-0.74	-361.19	2.99	y	n	y	y
20021215 12:45/1216 18:00	1.32	-479.48	1.53	y	n	n	n
20021217 16:30/1218 01:45	4.56	-393.99	2.49	y	n	y	y
20021220 01:30/1220 06:15	-1.21	-530.62	3.01	y	n	y	y

Continued on next page

Table 5 – *Continued from previous page*

Start/End	OMNI			Cluster SC3			
	B_z [nT]	V_x [km/s]	P $[cm^{-3}]$	B_z	V_x	n_{CIS}	n_{EFW}
20021223 02:15/1223 13:00	-2.32	-516.12	2.22	y	n	n	n
20021223 14:00/1223 22:30	0.89	-519.77	2.55	y	y	y	y
20021224 19:00/1225 01:45	0.88	-523.86	3.41	y	n	y	y
20021225 23:45/1226 07:15	-0.61	-414.38	2.21	y	y	n	n
20021226 23:00/1227 09:45	-1.79	-618.14	6.20	y	y	y	y
20021229 11:45/1229 17:00	-0.41	-580.12	2.39	y	n	n	n
20021230 17:45/1231 01:00	-1.01	-483.60	1.93	y	n	n	y
20021231 23:00/0101 05:15	0.60	-418.95	1.94	y	n	n	n
20030105 14:00/0105 21:00	-0.03	-414.46	1.69	y	n	n	n
20030106 23:15/0107 03:00	-1.62	-392.29	1.56	n	n	n	n
20030109 08:45/0109 16:15	1.45	-272.82	2.31	n	n	n	n
20030110 07:15/0110 15:15	-2.11	-401.03	2.72	y	n	y	y
20030111 08:15/0111 22:30	-0.20	-433.33	1.24	y	n	n	y
20030112 17:30/0113 00:15	1.53	-389.62	1.45	y	n	n	n
20030114 00:30/0114 08:30	-1.67	-388.53	2.27	y	n	n	y
20030116 10:15/0116 17:45	-1.20	-328.91	1.22	n	n	n	n
20030117 09:30/0117 13:30	-1.36	-327.09	2.55	y	y	y	y
20030118 23:30/0119 03:45	6.41	-459.46	4.82	y	y	y	y
20030119 21:00/0120 01:00	1.52	-597.95	2.38	y	n	y	y
20030121 06:30/0121 11:30	-1.77	-670.25	1.50	y	n	n	n
20030122 04:45/0122 09:30	0.11	-588.87	2.30	y	n	y	y
20030126 01:45/0126 06:30	-0.24	-713.82	2.75	y	y	y	y
20030127 08:15/0127 13:00	7.94	-509.30	0.47	y	n	y	y
20030128 12:30/0128 17:15	4.95	-443.83	4.15	y	y	y	y
20030130 19:45/0131 00:15	4.21	-510.33	2.63	y	n	y	y

Start/End	GUMICS Neutral Sheet
20020901 19:10/0901 23:54	–
20020906 14:07/0906 16:37	+
20020913 17:33/0913 20:06	+
20020918 12:47/0918 14:26	–
20020920 20:36/0921 02:13	+
20020928 02:58/0928 07:00	+
20021002 16:12/1002 23:52	–
20021014 12:34/1014 22:53	+
20021017 03:08/1017 04:11	–

998 **Table 6.** Intervals around the studied neutral sheet crossings in the tail. The Cluster SC3
 999 crossed the neutral sheet in all cases. The 3rd column shows whether the neutral sheet is visible
 1000 in the GUMICS–4 simulations.